

**Plasmon enhancement of luminescence upconversion**

| | |
|-------------------------------|--|
| Journal: | <i>Chemical Society Reviews</i> |
| Manuscript ID: | CS-REV-01-2015-000050 |
| Article Type: | Review Article |
| Date Submitted by the Author: | 20-Jan-2015 |
| Complete List of Authors: | Park, Wounjhang; University of Colorado, Electrical, Computer & Energy Engineering Lu, Dawei; University of Colorado, Ahn, Sungmo; University of Colorado, |
| | |

Plasmon Enhancement of Luminescence Upconversion

Wounjhang Park,^{1,2,*} Dawei Lu¹ and Sungmo Ahn¹

¹Department of Electrical, Computer and Energy Engineering

²Materials Science and Engineering Program

University of Colorado, Boulder, CO 80309-0425, U.S.A.

*Email: won.park@colorado.edu

Abstract:

Frequency conversion has always been an important topic in optics. Nonlinear optics has traditionally focused on frequency conversion based on nonlinear susceptibility but with the recent development of upconversion nanomaterials, luminescence upconversion has begun to receive renewed attention. While the upconversion nanomaterials open doors to a wide range of new opportunities, they remain too inefficient for most applications. Incorporating plasmonic nanostructures provides a promising pathway to highly efficient upconversion. Naturally, a plethora of theoretical and experimental studies have been published in recent years, reporting enhancements up to several hundred. It is however difficult to make meaningful comparisons since the plasmonic fields are highly sensitive to the local geometry and excitation condition. Also, many luminescence upconversion processes involve multiple steps via different physical mechanisms and the overall output is often determined by a delicate interplay among them. This review is aimed at offering a comprehensive framework for plasmon enhanced luminescence upconversion. We first present quantum electrodynamics descriptions for all the processes involved in luminescence upconversion, which include absorption, emission, energy transfer and

nonradiative transitions. We then present a bird's eye view of published works on plasmon enhanced upconversion, followed by more detailed discussion on comparable classes of nanostructures, the effects of spacer layers and local heating and the dynamics of plasmon enhanced upconversion process. Plasmon enhanced upconversion is a challenging and exciting field from the fundamental scientific perspective and also from the technological standpoints. It offers an excellent system to study how optical processes are affected by the local photonic environments. This type of research is particularly timely as the plasmonics is placing heavier emphasis on nonlinearity. At the same time, efficient upconversion could make significant impacts on many applications including solar energy conversion and biomedical imaging. The marriage of luminescent materials research with nanophotonics currently being initiated with the plasmon enhanced upconversion research explores a new frontier in photonics that could potentially spawn many exciting new fields.

1. Introduction

Frequency conversion has long been a topic of great interest in optics. Since the demonstration of second harmonic generation over a half-century ago,¹ nonlinear optics demonstrating a variety of frequency conversion mechanisms has become one of the greatest success stories in science, spawning a wide range of applications in information, medical, industrial, and military technologies.² Typically, frequency conversion is based on the nonlinear susceptibility which results in intensity dependent nonlinear refractive index and consequently enables a variety of frequency conversion mechanisms such as high harmonic generation, parametric oscillation and four-wave mixing. Despite the success, the frequency conversion by nonlinear susceptibility has a fundamental limitation in that it exhibits extremely low efficiency and thus requires phase matching with high-intensity, coherent light sources. In contrast, frequency conversion by optically active ions is known to be far more efficient than the nonlinear susceptibility based frequency conversion.^{3,4} It does not require phase matching and can be accomplished with incoherent light sources at low intensities. Thus, frequency upconverting phosphors activated with rare earth or transition metal ions are ideally suited for applications in lighting,⁵ displays,⁶ solar energy conversion,⁷ biosensing⁸ and biomedical imaging.^{9,10} More recently, novel applications such as security ink¹¹ and photoswitching¹² are being explored.

Although the upconversion phosphors are receiving renewed attention in recent years, they actually have a long history. Anti-Stokes emission which refers to the emission of photons with higher energy than the exciting photons is known by the 1960s. Excited state absorption (ESA) had already been treated in a textbook.¹³ With the rapid progress in laser spectroscopy, more complex upconversion mechanisms were discovered. Energy transfer upconversion (ETU)

was first observed in Yb^{3+} - Tm^{3+} codoped glass.¹⁴ In this mechanism, two sensitizer ions sequentially donate energy to a single activator ion by the Dexter-Förster energy transfer process,^{15,16} raising the activator to a higher excited state from which anti-Stokes emission originates.¹⁷ Additionally, cooperative sensitization¹⁸ and cooperative luminescence¹⁹ were also discovered at around the same time. The cooperative processes are distinguished from the ETU process in that they involve at least one virtual state. In cooperative sensitization, two sensitizers simultaneously transfer energy to an activator via a virtual intermediate state, raising the activator to a real excited state from which upconverted luminescence occurs. Cooperative luminescence is nearly the same as cooperative sensitization except that the emitting state is virtual instead of the intermediate state. In either case, the involvement of virtual states makes them much less efficient than the ETU process in which all participating states are real. The most recently discovered upconversion mechanism is photon avalanche.²⁰ In this process, the intermediate state from which ESA takes place is populated by cross relaxation with the terminating state of the luminescence process. The upconverted luminescence originating from the photon avalanche process is typically very weak at low pump power and rapidly increases at high pump power, exhibiting a sharp threshold.

Among the various upconversion mechanisms, ETU is known to be most efficient³ and will thus be the main focus of this review. It should however be noted that the theoretical framework we present in this review can be easily extended for other upconversion mechanisms such as ESA and triplet-triplet annihilation. Among the many systems exhibiting ETU, the rare earth ion pairs of Yb^{3+} - Er^{3+} and Yb^{3+} - Tm^{3+} exhibit efficient two- and three-photon ETU, resulting in green-red and ultraviolet-blue emissions, respectively. The ETU mechanism for luminescence upconversion in Yb^{3+} , Er^{3+} co-activated materials has been studied extensively.²¹⁻²⁶

The energy levels and major processes are shown schematically in Figure 1(a) and will be discussed in detail later. Briefly, incident light at 980 nm is mainly absorbed by Yb^{3+} ions, which then excites a nearby Er^{3+} ion into the $^4\text{I}_{11/2}$ level via Förster energy transfer process. Before the excited Er^{3+} ion decays, another Yb^{3+} ion may transfer energy to the Er^{3+} ion again, raising it to higher energy levels from which upconverted luminescence is emitted. The ETU process results in green and red emission in the $\text{Yb}^{3+}, \text{Er}^{3+}$ system, as shown in Figure 1(b). A photograph of green luminescence from colloidal solution of $\text{NaYF}_4:\text{Yb}^{3+}, \text{Er}^{3+}$ nanoparticles under 980 nm laser excitation is also shown in Figure 1(c). Like most lanthanide ions, the optical spectra of $\text{Yb}^{3+}-\text{Er}^{3+}$ and $\text{Yb}^{3+}-\text{Tm}^{3+}$ are largely insensitive to host materials and thus they exhibit ETU in a wide variety of host materials. While the host materials do not perturb the energy levels significantly, they could have profound impacts on nonradiative transition rates and consequently the ETU efficiency. Since the nonradiative transitions are generally mediated by phonons, host materials with low phonon energy tend to exhibit lower nonradiative transition rates and higher ETU efficiency. For this reason, fluorides are favored over oxides. The most efficient upconversion material is $\text{NaYF}_4:\text{Yb}^{3+}, \text{Er}^{3+}$ with energy conversion efficiencies up to $\sim 4\%$ at pump intensities around 1000 W/cm^2 .⁴

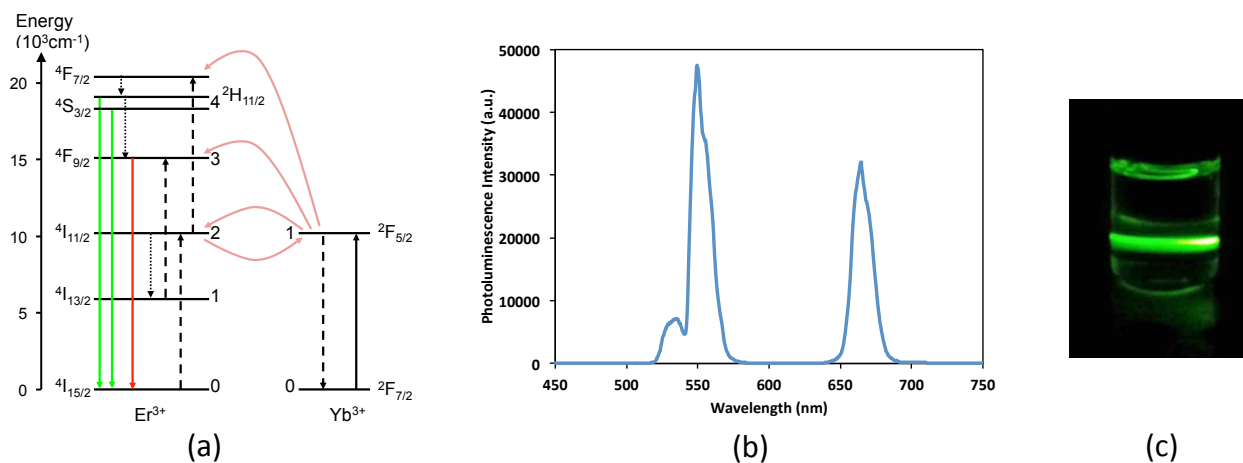


Figure 1. (a) Energy levels of Yb^{3+} and Er^{3+} ions relevant to the energy transfer upconversion process. Initial absorption is indicated by the black solid line arrow, subsequent energy transfer processes by the dashed arrows, non-radiative relaxations by dotted arrows and the final upconverted luminescence by the green and red arrows. Reprinted with permission from *ACS Nano* **2014**, *8*, 7780 (Ref. 93). Copyright (2014) American Chemical Society. (b) Photoluminescence spectrum of $\text{NaYF}_4: \text{Yb}^{3+}, \text{Er}^{3+}$ under 980 nm excitation. (c) Photograph of upconverted luminescence from a colloidal solution of $\text{NaYF}_4: \text{Yb}^{3+}, \text{Er}^{3+}$ nanoparticles under 980 nm excitation.

There are two different crystal structures NaYF_4 may form: cubic (α phase) and hexagonal (β phase). The hexagonal β - NaYF_4 crystal is known to exhibit higher upconversion efficiency. Figure 2 shows the schematic diagram of β - NaYF_4 crystal structure and the transmission electron micrographs (TEM) of β - NaYF_4 nanoparticles. The nanoparticles exhibit hexagonal shape arising from the hexagonal crystal structure and the high resolution TEM shows the interplanar spacing of 0.52 nm for the $(1,0,\bar{1},0)$ planes.²⁷ As shown in Figure 2(a), β - NaYF_4 has three cation sites.²⁸ The sites at $(0,0,0)$ (site B) and $(2/3, 1/3, 1/2)$ (site A) are coordinated by nine F^- ions forming tricapped trigonal prisms with point group symmetry C_{3h} . Site B is fully occupied by lanthanide (Ln^{3+}) ions whereas site A shows occupational disorder involving a 1:1 ratio of Na^+ and Ln^{3+} ions. The third cation site (site C), with irregular octahedral coordination, is half vacant and half occupied by Na^+ . The presence of two independent sites for Yb^{3+} and Er^{3+} ions in β - $\text{NaYF}_4: \text{Yb}, \text{Er}$ quadruples the number of possible $\text{Yb}^{3+} - \text{Er}^{3+}$ energy transfer pathways, leading to highly efficient ETU.²⁸ A key innovation that fueled the recent surge of research interest in the upconversion phosphors is the ability to synthesize highly monodispersed

nanoparticles. The synthesis of rare earth doped oxide nanoparticles has long been known.²⁹ However, oxides are not ideal hosts for upconversion phosphors as stated earlier, and oxide nanoparticles generally exhibit even poorer efficiencies than the bulk materials due to luminescence quenching by surface states. It was not until 2004 that efficient fluoride nanoparticle synthesis was reported.³⁰⁻³² These pioneering works were immediately followed by a plethora of refinements and improvements for morphology control, surface treatments, core-shell structures, etc.^{6,27,33-42} The huge potential for the upconversion nanomaterials is evident in the large number of review articles published in recent years.^{8,9,43-50} Despite the renewed interests and rapid progress being made, the upconversion efficiency of the currently available materials is not high enough for truly wide spread applications. As mentioned earlier, bulk materials show efficiencies of only a few percent and nanomaterials exhibit much poorer efficiency due to the large surface to volume ratio.⁵¹ It is therefore imperative to find ways to significantly improve the efficiency and the plasmonics offers a promising avenue for this, as shown in a recent review.⁴⁷

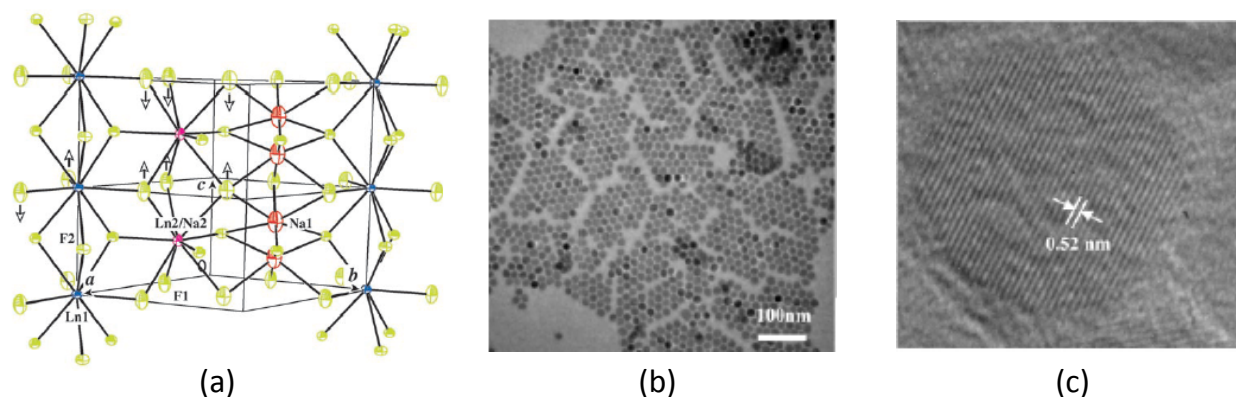


Figure 2. (a) Average structure of β - NaLnF_4 (Ln = Y, La–Lu) showing the three different columns of metal sites along c: Site A with a 1:1 mixture of Na2 and Ln2, site B with Ln1, both

with C_{3h} symmetric, tricapped trigonal-prismatic coordination geometry, and the Na1 site (site C) with C_3 symmetric, distorted octahedral coordination geometry. Local distortions owing to the disorder in the crystal are indicated by arrows. Reprinted with permission from *Angew. Chem. Int. Ed.* **2006**, 45, 2802. (Ref. 28). Copyright (2006) WILEY-VCH Verlag GmbH & Co. KGaA, Weinheim. (b) Transmission electron micrograph (TEM) and (c) high resolution TEM showing highly monodispersed hexagonal shape β -NaYF₄ nanoparticles with 0.52 nm interplanar spacing for the (1,0, $\bar{1}$,0) planes. Reprinted with permission from *ACS Nano* **2014**, 8, 7780 (Ref. 27). Copyright (2014) American Chemical Society.

Storing a fraction of its energy in electron gas, the surface plasmons are highly effective in creating a strongly localized and intense optical field which enhances a variety of optical processes. The best-known example is the surface enhanced Raman scattering. Using a rough silver surface, Raman scattering by a single molecule has been observed with enhancements up to a factor of 10^{14} .⁵²⁻⁵⁵ Much of the enhancement is believed to arise from the local field enhancement due to the hot spots produced by the silver nanostructure.^{56,57} Surface plasmon resonance can also be used to enhance luminescence⁵⁸⁻⁶⁸ and Förster energy transfer process.^{52,54,61,63} For luminescence upconversion, a recent theoretical study showed the enhancement of upconverted luminescence has a fourth power dependence on the local field enhancement, $|E_{loc}/E_0|^4$, in contrast to the quadratic dependence, $|E_{loc}/E_0|^2$, of luminescence enhancement.^{37,56} While the quenching issue still has to be dealt with, this raises the hope for dramatic enhancement in upconversion efficiency by the local field enhancement effect. Naturally, there has been a great deal of publications on plasmonic enhancement of upconverted luminescence, as documented later in this review. However, as commonly experienced with

newly emerging topics, there appears to be much confusion on what exactly the enhancement mechanism is and how much enhancement is achievable. For example, the reported enhancement factors in upconverted luminescence intensity vary widely between 0.25 and 450.^{69,70} There are many reasons for the discrepancies. Obviously, various geometries exhibiting different local field enhancement would lead to different enhancement factors. However, the upconversion efficiency itself is a function of excitation power and thus the enhancement factors from the same sample could vary widely depending on the experimental conditions, which are not always clearly described. Furthermore, ETU is a complex process involving multiple steps with distinct physical processes. Specifically, the enhanced local field can influence light absorption, emission and energy transfer. Therefore, enhanced upconverted luminescence does not always mean enhancement of energy transfer rate as often claimed and the enhancements of all involved processes must be carefully analyzed to fully understand their respective contributions and interplay between them. In this review, we first present a quantum electrodynamics based theoretical framework for all processes involved in ETU and their plasmon enhancement mechanisms. We will then provide an exhaustive and critical survey of plasmon enhanced upconversion research reported in recent years. Finally, the future prospect will be discussed.

2. Theoretical Foundation

2.1 Electron-Photon Interaction

In the quantum electrodynamics formalism, the Hamiltonian describing the interaction between electron and photon is given as,⁷¹

$$H_{\text{int}} = -\frac{e}{m} \mathbf{p} \cdot \mathbf{A} + \frac{e^2}{2m} |\mathbf{A}|^2 + e\phi \quad (1)$$

Here e and m are electronic charge and mass, \mathbf{p} is the canonical momentum of electron, and ϕ and \mathbf{A} is the scalar and vector potential of the electromagnetic field, respectively. According to Fermi's golden rule, the rate, W , of an electronic transition between two states, ψ_i and ψ_f , is given as,

$$W = \frac{2\pi}{\hbar} \left| \langle \psi_f | H_{\text{int}} | \psi_i \rangle \right|^2 \rho(\omega_f - \omega_i) \quad (2)$$

where $\hbar\omega_i$ and $\hbar\omega_f$ are the initial and final energy, respectively, and ρ is the density of states. Since the spatial variation of optical field takes place over a length scale (wavelength) much larger than the spatial extent of electronic wavefunctions (Bohr radius), one can take the Taylor expansion to obtain the well known multipolar Hamiltonian,⁷²

$$H_{\text{int}} = -\mathbf{d} \cdot \mathbf{E}_0 - \mathbf{m} \cdot \mathbf{B}_0 - \left[(\tilde{\mathbf{Q}} \nabla) \cdot \mathbf{E} \right]_0 + \dots \quad (3)$$

where \mathbf{d} , \mathbf{m} and \mathbf{Q} are electric dipole, magnetic dipole and electric quadrupole moments, respectively, and the subscript 0 represents the values evaluated at the position of the atomic nucleus. Magnetic dipole and electric quadrupole terms are generally many orders of magnitude smaller than electric dipole term and are ignored unless electric dipole transition is forbidden. This leads to the commonly adopted electric dipole approximation.

Most optical transitions in the lanthanide ions commonly employed in upconversion phosphors take place between $4f^n$ multiplets. The $4f$ shell of lanthanide ions is well shielded from the crystalline environment by the outer shell $5s$ and $5p$ electrons and thus the energy levels are largely insensitive to the host material. The crystalline environment can, however, make a profound impact on the optical transition rates. Most optical transitions of lanthanide ions are weakly allowed, exhibiting low absorption cross sections and long lifetimes. This is because all $4f^n$ multiplets have the same parity given by $(-1)^L$ where L is the total orbital angular

momentum quantum number. The electric dipole transition among the $4f^n$ multiplets is therefore forbidden by the parity selection rule. However, it was found that the optical transitions of lanthanide ions in most crystals are nonetheless electric dipole transitions. This is possible because an odd parity crystal field may cause mixing of a $4f^n$ state with another state with opposite parity, a $4f^{n-1}5d$ state in most cases, thereby relaxing the parity selection rule. Normally, this mixing has a negligible impact on energy levels but can profoundly change the transition rates. Using the second order perturbation theory, Judd and Ofelt derived the line strength as,

$$S_{ED}(J_i, J_f) = e^2 \sum_{t=2,4,6} \Omega_t \left| \langle f^n [\gamma SL] J \| U^{(t)} \| f^n [\gamma' S' L'] J' \rangle \right|^2 \quad (4)$$

where the $4f^n$ states are expressed in the Russell-Saunders scheme, $|f^n [\gamma SL] J J_z\rangle$, $U^{(t)}$ are the tensor operators containing both the crystal field and electric dipole operators, and Ω_t are the intensity parameters normally determined experimentally.^{73,74} The Judd-Ofelt theory had a great success in the past decades and correctly describes the weakly allowed nature of most lanthanide transitions. However, there remain transitions not explained well by the standard theory. These are often called the hypersensitive transitions because their intensities are highly sensitive to the host crystal.⁷⁵ A variety of mechanisms including lattice vibrations, electric quadrupole transition and inhomogeneous local field have been proposed but no consistent explanations have so far been found.

In addition to the direct optical transitions discussed above, any interaction between the optically active ions could strongly affect the overall transition rates. When two optically active ions are close to each other, Coulomb interaction between them must be considered. When the interionic distance, R , is large compared to the ionic radius, one can employ the standard perturbation technique and find that the first order correction is zero and the second order correction gives a term proportional to R^{-6} , which is the van der Waal's energy. While the van

der Waal's interaction results in a small, often negligible, correction to the electronic energy levels, it could lead to significant changes in transition rates by enabling energy transfer between ions.^{76,77} Following the time-dependent perturbation theory, the energy transfer rate between ions A and B is given by,

$$W_{ET} = \frac{2\pi}{\hbar} |\langle H_{AB} \rangle|^2 \int g_A(E) g_B(E) dE \quad (5)$$

Here g_A and g_B are the normalized emission and absorption spectra of the two ions, respectively, and their overlap integral determines the density of states of the combined system of ions A and B. The interaction Hamiltonian H_{AB} , if it is purely Coulombic, may be expanded in terms of spherical harmonics to obtain multipolar terms: dipole-dipole ($\propto R^{-6}$), dipole-quadrupole ($\propto R^{-8}$), and quadrupole-quadrupole ($\propto R^{-10}$), etc. Magnetic multipolar interaction is many orders of magnitude smaller than the electric counterpart and is thus neglected. Exchange interaction exhibits an exponential dependence on the interionic distance and is active only at extremely short distances. Therefore, it is generally believed that the energy transfer among most optically active ions and molecules is due mainly to the electric multipolar interaction. Energy transfer is responsible for numerous phenomena commonly observed in luminescent materials such as concentration quenching, cross relaxation, and sensitized luminescence.

2.2 Energy Transfer Upconversion

For a complete understanding of the ETU mechanism, one should set up rate equations containing all involved states and transitions. The energy level scheme of the prototypical Yb^{3+} - Er^{3+} system is shown in Figure 1(a). Yb^{3+} ion has 11 electrons in the $4f$ shell, forming a two level system with an absorption band centered at 980 nm. Most of the incident light is absorbed by the Yb^{3+} ions because they have much higher doping density and exhibit larger absorption cross-

section than the Er^{3+} ions.⁷⁸⁻⁸⁰ The absorption of the incident photon thus excites the Yb^{3+} ion into the $^2\text{F}_{5/2}$ level, from which the Yb^{3+} ion decays back to the ground level, $^2\text{F}_{7/2}$, through several different channels. It may decay radiatively, emitting an infrared photon, or nonradiatively by multiphonon emission. It is also possible to decay *via* the Förster energy transfer process, exciting a nearby Er^{3+} ion into the $^4\text{I}_{11/2}$ level. The excited state of Yb^{3+} ion ($^2\text{F}_{5/2}$) is resonant with the $^4\text{I}_{11/2}$ level of Er^{3+} and thus highly efficient energy transfer takes place between them, which is the first step of the ETU process. If the energy transfer takes place one more time before the excited Er^{3+} ion decays back to the ground state, the Er^{3+} ion is excited to the $^4\text{F}_{7/2}$ level and then quickly decays non-radiatively to the $^2\text{H}_{11/2}$ and $^4\text{S}_{3/2}$ levels from which the green luminescence occurs. A fraction of Er^{3+} ions in the $^4\text{S}_{3/2}$ state would decay non-radiatively into the slightly lower $^4\text{F}_{9/2}$ level where the red luminescence originates. An additional path for the red emission is for the Er^{3+} ion in $^4\text{I}_{11/2}$ level to decay nonradiatively into the $^4\text{I}_{13/2}$ level and then get excited to the $^4\text{F}_{9/2}$ level by the Förster energy transfer from a nearby Yb^{3+} ion. There are other processes that compete with the ETU process such as radiative and nonradiative decays from $^2\text{F}_{5/2}$ of Yb^{3+} and $^4\text{I}_{11/2}$ of Er^{3+} , energy transfer among Yb^{3+} ions (often called hopping), back energy transfer from Er^{3+} to Yb^{3+} , and cross-relaxation of Er^{3+} ion pairs. The cross relaxation of Er^{3+} ions offers a major quenching mechanism at high Er^{3+} concentrations.²⁶ Furthermore, there are three-photon upconversion processes, resulting in blue emission and also contributing to the green and red emission.²¹ However, it is expected that the three-photon processes make much smaller contributions than the two-photon processes except for very high pump powers.^{4,81} Therefore, the three-photon process may be omitted in the rate equations. Furthermore, the population of the $^4\text{F}_{7/2}$ level of Er^{3+} may be ignored as the relaxation from the $^4\text{F}_{7/2}$ level to the lower-lying $^2\text{H}_{11/2}$ and $^4\text{S}_{3/2}$ levels is known to be extremely fast.^{22,25,82-}

⁸⁵ Also, the $^2H_{11/2}$ and $^4S_{3/2}$ levels are close enough to be considered as a single level. With these slight simplifications, the complete set of rate equations can be written as,

$$\frac{dN_{D1}}{dt} = \sigma\Phi N_{D0} - W_{D10}N_{D1} + c_{Bd2}N_{A2}N_{D0} - c_{Fd2}N_{D1}N_{A0} - c_{d3}N_{D1}N_{A1} - c_{d4}N_{D1}N_{A2} \quad (6)$$

$$\frac{dN_{A1}}{dt} = W_{A21}N_{A2} - W_{A10}N_{A1} - c_{d3}N_{D1}N_{A1} \quad (7)$$

$$\frac{dN_{A2}}{dt} = c_{Fd2}N_{D1}N_{A0} - c_{Bd2}N_{A2}N_{D0} - c_{d4}N_{D1}N_{A2} - W_{A20}N_{A2} - W_{A21}N_{A2} \quad (8)$$

$$\frac{dN_{A3}}{dt} = W_{A43}N_{A4} + c_{d3}N_{A1}N_{D1} - W_{A30}N_{A3} \quad (9)$$

$$\frac{dN_{A4}}{dt} = c_{d4}N_{D1}N_{A2} - W_{A40}N_{A4} - W_{A43}N_{A4} \quad (10)$$

$$N_D = N_{D0} + N_{D1} \quad (11)$$

$$N_A = N_{A0} + N_{A1} + N_{A2} + N_{A3} + N_{A4} \quad (12)$$

Here N_i is the density of ions in the energy level i . The subscripts D1 and D0 represent the $^2F_{5/2}$ and $^2F_{7/2}$ levels of donor (Yb^{3+}), respectively, and A4, A3, A2, A1, and A0 indicate the $^4S_{3/2}$, $^4F_{9/2}$, $^4I_{11/2}$, $^4I_{13/2}$ and $^4I_{15/2}$ levels of acceptor (Er^{3+}), respectively. W is the decay rate and the subscript indicates the initial and final states of the transition. For example, W_{D10} is the decay rate of donor ion from D1 to D0 state. c_{d2} , c_{d3} and c_{d4} are the energy transfer coefficients for the energy transfer processes between the donor and the acceptor in A2, A3 and A4 levels, respectively. The additional subscripts, F and B, in the c_{d2} coefficient indicate the forward (donor to acceptor) and backward (acceptor to donor) energy transfers. Finally, N_D and N_A are the doping densities of donor and acceptor, respectively, σ is the absorption cross section of the donor ion, and Φ is the incident light flux. It is noted that we consider only the backward transfer

from the acceptor $^4I_{11/2}$ level to donor as the lifetimes of the higher excited states of the acceptor are so short that backward transfer is negligible. Also, the decay rate, W , should in general include the rates of both radiative and nonradiative decays. In bulk $\text{NaYF}_4:\text{Yb}^{3+},\text{Er}^{3+}$ samples, the major nonradiative decay channel is multiphonon emission, but thanks to the small phonon energy of the fluoride host, the nonradiative decay rate is usually small. Hence, W may generally be replaced with the radiative decay rate. In the plasmon enhanced upconversion, however, the upconverting material is in close proximity of metal surface and the energy transfer to metal offers a highly efficient nonradiative decay channel. Therefore, nonradiative decay rate should not only be included but could very well dominate. This should be kept in mind in the analysis of plasmon enhanced upconversion.

Since the rate equations above are rather unwieldy, it is natural to seek for further simplifying approximations. Many groups have ignored the red emission entirely.^{22,82,83,86,87} Others assumed fast equilibrium between the $^2F_{5/2}$ level of Yb^{3+} and the $^4I_{11/2}$ level of Er^{3+} .^{4,22,56,83,88} And yet other groups ignored the backward energy transfer from Er^{3+} to Yb^{3+} .^{41,87-90} However, the justifications for these approximations are often dubious. Literature shows that the red emission is clearly not negligible and is often dominant at high excitation power densities. The assumption of fast equilibrium requires that the energy transfer coefficients, c_{Fd2} and c_{Bd2} , are so large that the forward and backward energy transfer rates are much greater than the radiative and nonradiative decay rates. Ignoring backward energy transfer means $c_{Fd2} \gg c_{Bd2}$, which is at odds with the assumption of fast equilibrium. The problem lies in the difficulty of directly measuring the energy transfer coefficients. There is naturally a dearth of data on energy transfer coefficients. However, the few that reported the values of energy transfer coefficients indicate that c_{Fd2} and c_{Bd2} are of the same order of magnitude^{82,86,91,92} and the

energy transfer rates may be comparable to the decay rates.^{82,86,92} Although the values of energy transfer coefficients depend strongly on the doping densities and the host material, the approximations mentioned above appear to be poorly justified and we therefore proceed with the full set of rate equations (6)~(12) and seek solutions in the weak and strong excitation limits. The details on how to obtain steady-state solutions of the rate equations in the weak and strong excitation limits are given elsewhere.⁹³ Briefly, the essence of the approximations made for weak and strong excitation limits is to consider the competition between the upconversion and decay processes for the intermediate energy levels, $^2F_{5/2}$ of Yb^{3+} and $^4I_{11/2}$ of Er^{3+} . In the weak excitation regime, decay processes dominate while the upconversion processes become dominant in the strong excitation regime. These approximations allow significant simplifications and offer simple and revealing solutions. In the weak excitation limit, the green and red photon emission rates (in units of per volume per time) are given as,

$$\Phi_G = \frac{W_{A40}}{W_{A4}} \frac{c_{d4} c_{Fd2} N_A N_D}{c_{Bd2} W_{D10}^2} \cdot (\sigma\Phi)^2 \quad (13)$$

$$\Phi_R = \left(\frac{W_{A43} c_{d4}}{W_{A4}} + \frac{W_{A21} c_{d3}}{W_{A10}} \right) \frac{c_{Fd2} N_A N_D}{c_{Bd2} W_{D10}^2} \cdot (\sigma\Phi)^2 \quad (14)$$

Here the W_{A4} is the total decay rate of energy level A4, $W_{A4} = W_{A40} + W_{A43}$. Equations (13) and (14) clearly show the quadratic dependence on the incident photon flux, which is a consequence of the two-photon process responsible for upconversion. In addition, they show the upconverted luminescence intensity should increase linearly with the donor and acceptor densities. Also, the upconverted luminescence intensity varies linearly with the energy transfer coefficients, c_{Fd2} and c_{d4} , and inversely with c_{Bd2} and the square of donor decay rate, W_{D10} . In the strong excitation limit, the green and red photon emission rates are found to be,

$$\Phi_G = \frac{W_{A40} N_{D0}}{W_{A4} 2} \sigma \Phi \quad (15)$$

$$\Phi_R = \frac{W_{A43} N_{D0}}{W_{A4} 2} \sigma \Phi \quad (16)$$

Equations (15) and (16) show the linear power dependence on the excitation power density. Also, it is important to note that the upconverted luminescence intensity depends only on the donor density and excitation power density but not on any of the energy transfer coefficients since, in the strong excitation limit, the energy transfer rate is so fast that the upconversion is limited by the absorption by the donor ion.

2.3 Plasmon Enhancement of Upconversion

The expressions in equations (13)~(16) provide the basis for determining the plasmon enhancement effects on the various processes involved in upconversion. The parameters that can be affected by surface plasmon are the decay rates (W 's), energy transfer coefficients (c 's) and the absorption cross section, σ . These parameters represent the three types of processes involved in ETU: decay (radiative and nonradiative), energy transfer and absorption. We now discuss how these processes may be influenced by surface plasmon, starting with the absorption cross section, σ . Absorption may be calculated classically from the Poynting's theorem, which states that the divergence of the Poynting vector specifies the power dissipation in an absorbing medium. Thus, for monochromatic light, the power dissipation is given by,⁹⁴

$$P_{abs} = \frac{1}{2} \int_V \omega (\epsilon'' |\mathbf{E}|^2 + \mu'' |\mathbf{H}|^2) dV \quad (17)$$

where ϵ'' and μ'' are the imaginary part of permittivity and permeability, respectively.

Normally, $\mu'' = 0$ at optical frequencies and we only need to consider the electric part. Now we

transform equation (17) into a form appropriate for optically active ions characterized by polarizability rather than continuous absorbing medium specified by permittivity. For this, we first rewrite the power dissipation in terms of current density, \mathbf{j} ,

$$P_{abs} = \frac{1}{2} \int_V \text{Re} \{ \mathbf{j}^* \cdot \mathbf{E} \} dV \quad (18)$$

In the dipole approximation, the current density can be expressed in terms of the induced dipole moment, \mathbf{d} , as $\mathbf{j} = -i\omega\mathbf{d}\delta(\mathbf{r} - \mathbf{r}_0)$, which yields,

$$P_{abs} = \frac{\omega}{2} \text{Im} \{ \mathbf{d}^* \cdot \mathbf{E}(\mathbf{r}_0) \} \quad (19)$$

where $\mathbf{E}(\mathbf{r}_0)$ is the external electric field at the position of the ion. Since the induced dipole moment is given by the polarizability, $\mathbf{d} = \alpha\mathbf{E}$, the absorbed power may now be written as,

$$P_{abs} = \frac{\omega}{2} \text{Im} \{ \alpha \} |\hat{\mathbf{n}}_d \cdot \mathbf{E}(\mathbf{r}_0)|^2 \quad (20)$$

where $\hat{\mathbf{n}}_d$ is the unit vector along the direction of the induced dipole moment, \mathbf{d} . The absorption cross section is defined as the ratio of the absorbed power to the incident intensity,

$$\sigma = \frac{P_{abs}}{I_{inc}} = c\mu_0\omega \text{Im} \{ \alpha \} \frac{|\hat{\mathbf{n}}_d \cdot \mathbf{E}(\mathbf{r}_0)|^2}{|\mathbf{E}_0|^2} \quad (21)$$

where \mathbf{E}_0 is the incident field amplitude. The polarizability is determined by the transition matrix element and thus the electronic wavefunctions only. Therefore, plasmon resonance enhances absorption by the local field enhancement and equation (21) shows absorption cross section is enhanced as $|E/E_0|^2$. We note that the polarizability may depend on the external field in the strong coupling limit. However, to our knowledge, there has not been any work on plasmon enhanced upconversion in the strong coupling limit and we thus treat polarizability as a purely electronic property in this review.

Radiative and nonradiative decay rates are affected differently by the plasmonic fields. Radiative decay rates depend on the density of states as shown in equation (2). In quantum electrodynamics, we should consider the states of the combined system of atom and photon and thereby the density of states in equation (2) includes the photon states as well as the electronic states. Consequently, the large increase in photon density of states by the introduction of a large number of evanescent modes supported by surface plasmon increases the optical transition rate. This was first recognized by Purcell⁹⁵ in 1946 and has been the main inspiration of cavity quantum electrodynamics, which remains an active research topic.⁹⁶ The Purcell effect in plasmonic nanostructures has been studied recently by several groups.^{97,98} The theoretical description of the Purcell effect can be derived from the Fermi's golden rule. In the dipole approximation, the radiative decay rate is found from equation (2) using the dipole term of the multipolar Hamiltonian with vacuum electric field,⁷¹

$$W = \frac{\pi\omega}{3\hbar\epsilon} |\mathbf{d}|^2 \rho(\mathbf{r}_0, \omega) \quad (22)$$

where \mathbf{r}_0 is the position of the emitter. Classically, the radiation rate of a dipole emitter can be calculated from the power dissipation rate according to the Poynting's theorem,

$$P_{rad} = -\frac{1}{2} \int_V \text{Re} \{ \mathbf{j}^* \cdot \mathbf{E} \} dV \quad (23)$$

Expressing the current density in terms of the induced dipole moment, just as before, yields,

$$P_{rad} = \frac{\omega}{2} \text{Im} \{ \mathbf{d}^* \cdot \mathbf{E}(\mathbf{r}_0) \} \quad (24)$$

Note that although equation (24) is formally identical to equation (19) they have different physical meaning. The electric field in equation (19) represents the incident field while the electric field in equation (24) is the dipole field. Expressing the dipole field in terms of the dyadic Green function gives,

$$P_{rad} = \frac{\omega^3}{2c^2\epsilon} \left[\mathbf{d} \cdot \text{Im} \{ \vec{\mathbf{G}}(\mathbf{r}_0, \mathbf{r}_0; \omega) \} \cdot \mathbf{d} \right] \quad (25)$$

Comparing equations (22) and (25) allows us to write the density of states in terms of the dyadic Green function,

$$\rho(\mathbf{r}_0, \omega) = \frac{6\omega}{\pi c^2} \left[\hat{\mathbf{n}}_d \cdot \text{Im} \{ \vec{\mathbf{G}}(\mathbf{r}_0, \mathbf{r}_0; \omega) \} \cdot \hat{\mathbf{n}}_d \right] \quad (26)$$

It is noted that \mathbf{d} represents the quantum mechanical transition matrix element in equation (22) but is a classical dipole in equation (25). This leads to a discrepancy between the quantum mechanical and classical expressions by a constant factor.⁹⁹ It is therefore customary to evaluate the enhancement factor, often called the Purcell factor, given as the ratio of radiation rates in a nanophotonic environment and free space, for which the classical and quantum mechanical calculations should agree. The density of states given in equation (26) is the correct quantum mechanical expression and is often called the partial density of states. The total density of states can be obtained by averaging over all possible dipole orientations. With equations (22)~(26), it is now possible to predict the enhancement in radiative decay rate by evaluating the dyadic Green function for a given plasmonic nanostructure.

Nonradiative decay such as multiphonon emission is not directly impacted by the plasmonic fields. However, the presence of metal can introduce additional nonradiative decay channels, effectively increasing the nonradiative decay rate and consequently resulting in luminescence quenching. The additional nonradiative decay rate may be calculated by evaluating the ohmic loss in the environment for the field emitted by a radiating dipole,^{100,101}

$$\frac{W_{nr}}{W_0} = \frac{1}{P_0} \frac{1}{2} \int_V \text{Re} \{ \mathbf{j}^* \cdot \mathbf{E} \} dV \quad (27)$$

Here W_0 is the free space decay rate, P_0 is the radiation rate of a classical dipole,

$P_0 = \omega^4 |\mathbf{d}|^2 / 12\pi\epsilon_0 c^3$, in free space, and the integral is performed over the metal volume. Also, \mathbf{E}

is the field emitted by the dipole emitter and \mathbf{j} is the current density induced by the emitted field.

They can be expressed in terms of the dyadic Green function as follows.

$$\mathbf{j} = \omega\epsilon''\mathbf{E} \quad (28)$$

$$\mathbf{E}(\mathbf{r}) = \frac{\omega^2}{c^2\epsilon} \vec{\mathbf{G}}(\mathbf{r}, \mathbf{r}_0; \omega) \cdot \mathbf{d} \quad (29)$$

Just like the radiative decay rate, the dyadic Green function allows us to estimate the changes in the nonradiative decay rate. The interplay among the absorption, radiative and nonradiative decays is illustrated in Figure 3 in which the excitation (absorption), radiative and nonradiative decay rates for a fluorescence molecule near a gold nanoparticles are plotted.¹⁰¹ As shown in Figure 3(a), the excitation rate increases as the molecule is placed closer to the gold nanoparticle, following the $|E/E_0|^2$ scaling given in equation (21). The quantum yield however decreases with decreasing separation distance, signifying the corresponding increase in nonradiative decay rate given in equation (27). The rapid increase in nonradiative decay rate results in the emission rate peaking at a short distance away from the nanoparticle, as shown in Figure 3(b). It defines the optimal spacer layer thickness that needs to be incorporated in most plasmonic nanostructures aimed at enhancing luminescence.

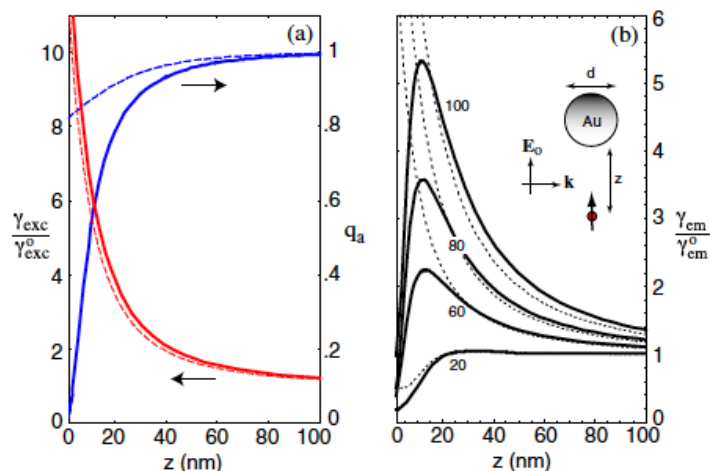


Figure 3. Calculated quantum yield q_a , excitation rate γ_{exc} , and fluorescence rate γ_{em} as a function of the separation distance between gold nanoparticle and fluorescent molecule. γ_{exc} and γ_{em} are normalized with their corresponding free-space values ($z \rightarrow \infty$). The solid curves are the result of multiple multipole calculations⁷¹ whereas the dashed curves correspond to the dipole approximation in which all higher order multipoles of gold nanoparticles were ignored. In (a) the particle diameter is $d = 80$ nm and in (b) it is indicated in the figure. Excitation wavelength is $\lambda = 650$ nm and $\epsilon = -2:99 + i1:09$ (gold). Reprinted with permission from *Phys. Rev. Lett.* **2006**, *96*, 113002 (Ref. 101). Copyright (2006) American Physical Society.

Finally, we describe the rate of energy transfer. For simplicity, we assume dipole-dipole coupling and estimate the Förster energy transfer rate, which in a dispersive and absorbing medium is given by^{102,103}

$$W_{ET} = \int d\omega g_A(\omega) g_D(\omega) \tilde{w}(\omega) \quad (30)$$

where g_A and g_D are the free-space normalized absorption and emission spectra of acceptor and donor ions, respectively. The information about the medium is lumped into the transition rate, $\tilde{w}(\omega)$, which can be expressed in terms of the dyadic Green function as follows.

$$\tilde{w}(\omega) = \frac{2\pi}{\hbar^2} \frac{\omega^2}{\epsilon_0 c^2} \left| \mathbf{d}_A^* \cdot \tilde{\mathbf{G}}(\mathbf{r}_A, \mathbf{r}_D, \omega) \cdot \mathbf{d}_D \right|^2 \quad (31)$$

Here, \mathbf{d}_A and \mathbf{d}_D are the dipole moments of acceptor and donor ions, respectively; \mathbf{r}_A and \mathbf{r}_D indicate the positions of acceptor and donor ions, respectively. Like the radiative and nonradiative decay rates, we now have expressed the Förster energy transfer rate in terms of the dyadic Green function. The rigorous evaluation of the dyadic Green function is however non-trivial and the theoretical works have so far been carried out mostly for highly symmetric shapes like planar surface, sphere and ellipsoid.¹⁰³⁻¹⁰⁹ An earlier study observed enhanced Förster energy transfer rate in optical cavities and attributed it to the enhanced local density of states to which the donor emission rate is directly proportional.^{102,103,106} From equation (26), we know the donor emission rate is proportional to the imaginary part of the dyadic Green function $\mathbf{G}(\mathbf{r}_D, \mathbf{r}_D, \omega)$. For a small donor-acceptor distance, $\mathbf{G}(\mathbf{r}_A, \mathbf{r}_D, \omega)$, may be similar to $\mathbf{G}(\mathbf{r}_D, \mathbf{r}_D, \omega)$. However, the real part of the dyadic Green function often dominates over the imaginary part and thus the energy transfer enhancement is generally quite different from the radiative decay rate enhancement. In fact, it has recently been shown that the energy transfer enhancement is not related to the density of states enhancement.^{104,105} Theoretical studies indicate that the energy transfer enhancement is generally smaller than the spontaneous emission enhancement, although the enhancement depends strongly on the donor-acceptor distance.^{77,103,106} Figure 4 shows the energy transfer rate enhancement calculated with equations (30) and (31) for an ion pair in the vicinity of a flat silver surface. It shows the energy transfer rate is enhanced at frequencies slightly below the surface plasmon frequency while it is suppressed at frequencies above it. The enhancement factor is higher when closer to the metal surface. Also, the enhancement factor is high for large separation distances. For short separation distances, the energy transfer rate is already very high and is difficult to enhance further. It has been experimentally observed that the Förster energy transfer

rate can be significantly enhanced in the vicinity of plasmonic structures.^{52,110-115} We should expect that most of the observed plasmon enhancement in energy transfer rate come from the enhancement of originally slow energy transfer rate between donor-acceptor pairs with large separation.

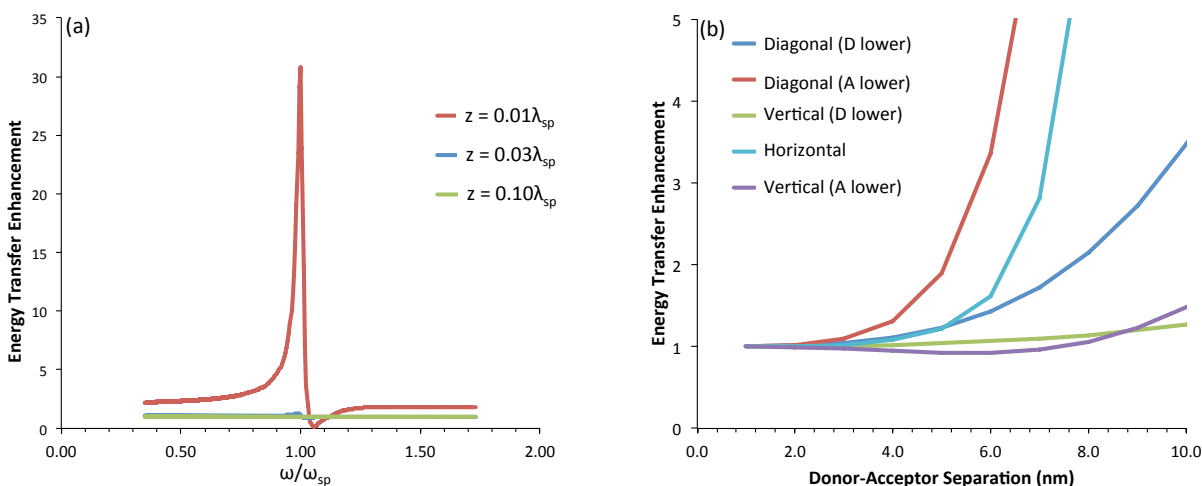


Figure 4. (a) Energy transfer rate enhancement factor calculated for a donor-acceptor pair with a pair separation of 3.4 nm placed at various distances, z , from a flat silver surface. ω_{sp} and λ_{sp} represent the surface plasmon frequency and wavelength, respectively. (b) Energy transfer rate enhancement factor as a function of donor-acceptor distance. The donor is placed at $0.03\lambda_{sp}$ away from the metal surface. In the legend, horizontal, diagonal and vertical represent the orientation and arrangement of donor and acceptor dipoles corresponding to G_{xx} , G_{yy} , G_{xz} , G_{zx} , and G_{zz} in equation (31). Reprinted with permission from *ACS Nano* **2014**, *8*, 7780 (Ref. 93). Copyright (2014) American Chemical Society.

We have established quantum electrodynamic foundation for all optical processes involved in ETU, which provide quantitative predictions on how surface plasmon can enhance or

suppress upconversion. We can now return to equations (13)~(16) to determine the plasmon enhancement effects on the various processes involved in ETU. The expressions for the green emission are a bit simpler as it has only one possible excitation pathway while the red emission has two different excitation pathways as well as possible three-photon processes. We will therefore examine the enhancement of the green luminescence for simplicity and clarity, noting that the analysis can be extended to red luminescence in a straightforward fashion. Equation (15) shows the plasmon could impact the upconverted luminescence intensity through the radiative efficiency, W_{A40}/W_{A4} and absorption cross section, σ , in the strong excitation limit. The absorption enhancement is described clearly by equation (21). The behavior of the radiative efficiency is much more complex. First, we may assume the nonradiative decay rate, W_{A43} , is not influenced by surface plasmon. W_{A40} can be enhanced by the Purcell effect as given in equation (25). And the metal surface will introduce an additional nonradiative decay rate, W_{nr} , described by equation (27), which represents quenching. Therefore the radiative efficiency in a plasmonic nanostructure may be written as

$$\left(\frac{W_{A40}}{W_{A4}}\right)_{sp} = \frac{F_P W_{A40}}{F_P W_{A40} + W_{A43} + W_{nr}} \quad (32)$$

where F_P is the Purcell factor for the green emission. The enhancement factor for the radiative efficiency is then given as,

$$F_{rad} = \left(\frac{W_{A40}}{W_{A4}}\right)_{sp} / \left(\frac{W_{A40}}{W_{A4}}\right) = \frac{W_{A40} + W_{A43}}{W_{A40} + (W_{A43} + W_{nr})/F_P} \quad (33)$$

It is immediately seen that the Purcell effect would make a significant impact only for originally inefficient materials. That is, the radiative efficiency is enhanced substantially only when $W_{A43} + W_{nr}$ is much larger than W_{A40} . In the limit of an infinitely large Purcell factor, the radiative

efficiency enhancement saturates at $1 + W_{A43}/W_{A40}$. We may therefore conclude that generally the Purcell enhancement of upconverted luminescence would make only a modest contribution. This is because when the radiative decay rate becomes high the emission rate is limited by the upconversion rate. We note that there is also an intrinsic nonradiative decay via multiphonon emission or phonon-assisted energy transfer to defects. In fluorides, this should be small as stated earlier. It may become more substantial in nanoparticles due to surface defects. In any case, the intrinsic nonradiative decay rate does not depend on the presence of metal and it is straightforward to incorporate it in the above equations.

The dominant contribution to the upconversion enhancement therefore comes from absorption enhancement, F_a , which is proportional to the square of local field enhancement. Thus the overall enhancement factor for the green luminescence intensity in the strong excitation limit is,

$$F_{strong} \approx F_a \quad (34)$$

In the weak excitation limit, equation (13) shows that we have to consider the energy transfer coefficients, c_{d4} , c_{Fd2} , and c_{Bd2} , and the infrared decay rate, W_{D10} , in addition to the radiative efficiency and absorption cross section. Since the radiative efficiency should not be affected significantly, the overall enhancement factor, F_{weak} , for the green luminescence intensity in the weak excitation limit can be written as

$$F_{weak} \approx \frac{F_{d4} F_{Fd2} F_a^2}{F_{Bd2} F_{D10}^2} \quad (35)$$

where F_{d4} , F_{Fd2} and F_{Bd2} are the enhancement factors for the energy transfer processes represented by the coefficients c_{d4} , c_{Fd2} , and c_{Bd2} , respectively, and F_{D10} is the enhancement factor for the infrared decay rate, W_{D10} , of the donor ion. W_{D10} can be enhanced by the Purcell effect and also by the additional nonradiative decay rate introduced by metal. Either way any

increase in the donor decay rate is detrimental to the upconversion, as it reduces the population of the intermediate level from which upconversion takes place. For the energy transfer enhancement, there are two reasons we should expect F_{Fd2} and F_{Bd2} would cancel each other out. First, in most upconversion phosphors, the doping densities are extremely high. In $\text{NaYF}_4:\text{Yb}^{3+},\text{Er}^{3+}$, the doping densities for Yb^{3+} and Er^{3+} are typically 18% and 2%, respectively. These densities lead to mean donor-acceptor distance less than 1 nm. At such a short distance the energy transfer rate is very high and it is extremely difficult to further enhance it. It is therefore reasonable to assume $F_{Bd2} = F_{Fd2} = 1$. Furthermore, even if there is enhancement, the two energy levels of donor and acceptor are nearly resonant and the forward and backward energy transfer processes are expected to be enhanced the same way, $F_{Bd2} = F_{Fd2}$. Thus the enhancement factor in the weak excitation limit may be simplified to,

$$F_{weak} \approx \frac{F_d F_a^2}{F_{D10}^2} \quad (36)$$

Based on the analysis given above, we may draw a few conclusions. As stated earlier, even with extremely high Purcell enhancement, the green emission would not be enhanced significantly. Instead, equations (34)~(36) show that the processes occurring at the excitation wavelength, absorption, energy transfer and the donor decay, are important for the overall enhancement of upconversion. It is therefore desirable to place the plasmon resonance at the excitation wavelength rather than the emission wavelength. As shown later, the vast majority of papers published so far deal with plasmon enhancement of emission. It is only recently that plasmon resonant with the excitation wavelength has begun to receive attention. Also, in the weak excitation limit, the upconverted luminescence intensity is enhanced linearly to energy transfer enhancement and quadratically to absorption enhancement. The quadratic dependence on absorption enhancement arises from the nonlinear nature of the upconversion process and

promises a potentially very high enhancement. In the strong excitation limit, however, the enhancement is due mostly to absorption enhancement. Thereby, the plasmon enhancement would have the biggest impact on applications like solar energy conversion or imaging where the excitation power is typically low. Finally, any increase in the donor decay rate, whether radiatively or nonradiatively, could severely curtail the overall enhancement as the enhancement factor decreases quadratically to the donor decay rate enhancement. Thus, designing a plasmonic nanostructure with high absorption enhancement and yet weak Purcell effect for the infrared emission is important. Also, it is critical to minimize quenching due to the metal surface.

3. Experimental Studies on Plasmon Enhanced Upconversion

Based on the theoretical framework laid out in the previous section, we can now discuss the experimental results reported to date. There is a large and growing body of experimental studies on plasmon enhanced upconversion reporting a wide variety of structures and measurement conditions. Such wide variations in geometry and excitation conditions make it very difficult to have direct comparisons. A major difficulty is, as explained in detail in the previous section, that the enhancement is dependent on the excitation condition. The theoretical analysis presented in the previous section clearly shows that, when the excitation power is low, the upconversion efficiency scales linearly with the excitation power, just as any other two-photon processes. As the excitation power is increased, the ETU process saturates and exhibits a constant efficiency independent of the excitation power. This was clearly shown in a recently work on $\text{NaYF}_4:\text{Yb}^{3+},\text{Er}^{3+}$ nanoparticles deposited on silver nanograting that supports surface plasmon polariton at 980 nm.⁹³ As shown in Figure 5, the upconverted luminescence intensity follows a power law dependence on the pump power density. Both the reference and

plasmonically enhanced samples scaled quadratically with the pump power density in the weak excitation region and linearly in the strong excitation region. The effect of surface plasmon is to shift the intensity curves to the low power densities due to the local field enhancement, which result in enhanced local optical power density. While the exact amount of the shift should be determined by the theoretical analysis given in the previous section, it is clear that the enhancement factor should be dependent on the pump power. As shown in Figure 5(c), the enhancement factor for green emission varied from 3.1 to 16.0 while the red emission enhancement factor changed from 4.2 to 38.8. The enhancement factor is independent of excitation power in the low and high power limits while it changes rapidly in the intermediate region. It is therefore imperative to specify the excitation power density when reporting enhancement in upconversion. Furthermore, it is generally easier to achieve large enhancement when the original efficiency is poor. Energy transfer rate, for example, can be enhanced greatly when the donor-acceptor distance is large and thus the energy transfer rate is originally small. For short distances, however, the energy transfer rate is already very high and it is difficult to achieve any further enhancement, as shown in Figure 4(b). The same is generally true for absorption and emission enhancement as well. It should be therefore noted that enhancement factor is often misleading and not an ideal quantity to characterize plasmon enhancement of upconversion.

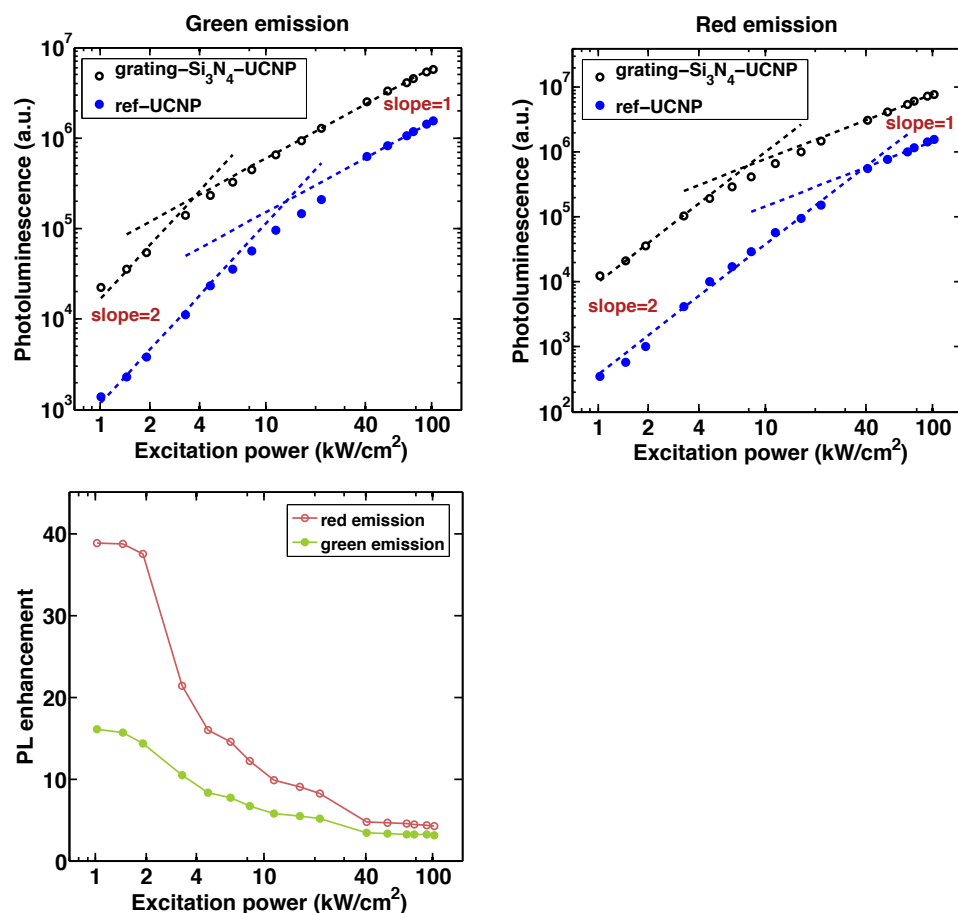


Figure 5. (a) Green and (b) red photoluminescence intensities under various excitation power densities. The UCNP on silver nanograting is denoted with black open circles while the reference sample on flat metal film is represented by blue filled circles. The blue and black dash lines are obtained by the least-square fitting with the slopes of 1 and 2 as denoted. (c) Enhancement factors of the green (green filled circles and line) and red (red open circles and line) upconverted luminescence as a function of the excitation power density. Reprinted with permission from *ACS Nano* **2014**, 8, 7780 (Ref. 93). Copyright (2014) American Chemical Society.

Nevertheless, enhancement factor is one parameter almost universally reported in the literature, often without proper description of experimental conditions. In this review we attempt

to provide scientifically meaningful context to the increasingly numerous yet scattered data in the literature. Figure 6 summarizes the enhancement factors reported in a variety of structures, which are broadly classified into glass composites, nanoparticles (including nanowires and other shapes), nanoparticle arrays, core-shells, island films and periodically patterned structures. The reported enhancement factor varies widely from less than unity (quenching) to several hundred. Even within the same class of structures, wide variations are observed. It should be kept in mind that the data include many different types of upconversion systems including Yb-Er, Yb-Tm, Yb-Ho and Er singly doped upconversion systems. Another obvious variation is in the plasmon resonance wavelength, which should drastically affect the enhancement as discussed earlier. Within the same class exhibiting plasmon resonance at the same wavelength, the enhancement should depend on the precise geometry and the excitation conditions. Despite the lack of details, Figure 6 nonetheless provides a bird's-eye view of the field from which some helpful insight can be extracted. First, the enhancement factor ranges mostly from 1 to 100, with only a few exceeding 100. This may be due to the fact that the majority of the studies used plasmon resonances matched to the emission wavelength and did not take advantage of potential enhancement in absorption and energy transfer. Another possible contributing factor is the use of high excitation power, which generally yields higher luminescence intensity but lower enhancement factor. The luminescence quenching by metal should always be a factor, although it may be reduced by incorporating a spacer layer. Secondly, gold appears to be just as effective as silver. Gold exhibits higher intrinsic loss than silver in the visible frequency region and should in principle provide weaker plasmon resonance and stronger quenching. But the experimental data compiled in Figure 6 do not show any clear advantage for silver. In fact, the highest enhancement factors were all reported with gold. We provide more detailed information on the

studies reporting enhancement factors greater than 10 in Table 1. In the following sections, we present more in-depth discussion on various categories.

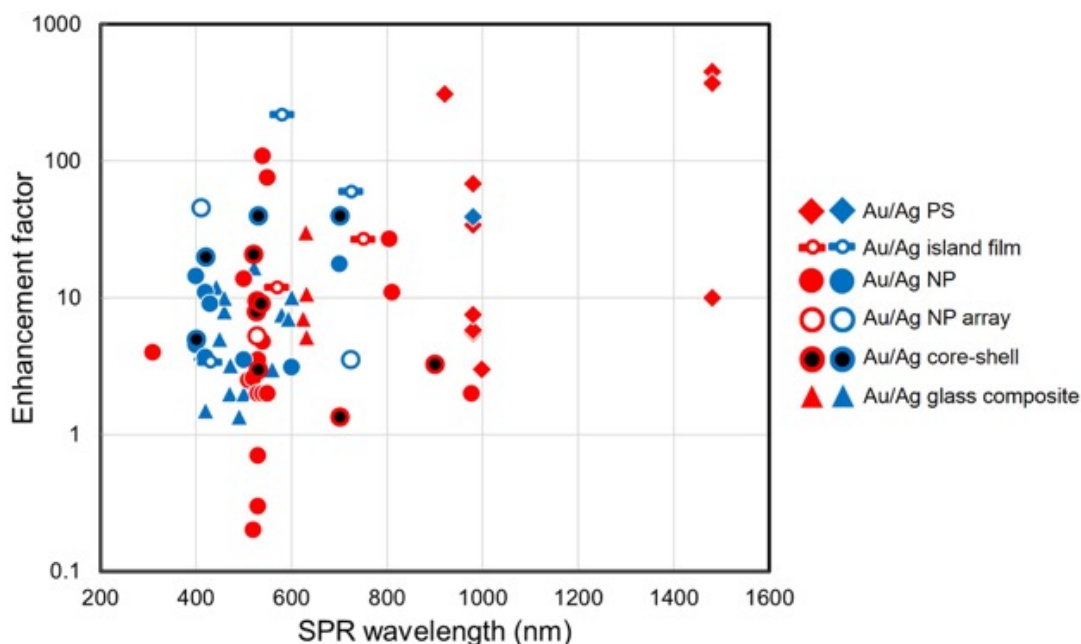


Figure 6. Upconversion luminescence enhancements as a function of surface plasmon resonance wavelength, reported for various geometries and materials. Gold and silver are represented as yellow and gray colors, respectively. The various plasmonic geometries include glass composites (triangle), nanoparticles such as nanosphere, nanorod, nanowire, nanoprism etc. (circle), self-assembled nanoparticle array (ring), core-shell (concentric circle), island film or flat film (horizontal bar with circle), and periodic structure (diamond).

| | Material | SPR (nm) | green | red | blue | other | max | Ref |
|--|----------|----------|---------|------|---------|----------------|------|-----|
| Au/Ag PS | | | | | | | | |
| Square aperture array | Au | 1480 | - | - | - | 450 (980 nm) | 450 | 117 |
| Annular aperture array | Au | 1480 | - | - | - | 370 (980 nm) | 370 | 117 |
| Disk-coupled dots-on-pillar antenna array | Au | 920 | 100 | 310 | - | - | 310 | 61 |
| Pyramid array | Au | 980 | 68 | 5.8 | - | - | 68 | 90 |
| Nanograting array | Ag | 980 | 16 | 39 | - | - | 39 | 93 |
| Nanohole array | Au | 980 | 32.6 | 34 | - | - | 34 | 58 |
| Annular aperture array | Au | 1480 | - | - | - | 10 (980 nm) | 10 | 117 |
| Au/Ag island film | | | | | | | | |
| Ag island film | Ag | 580 | 220 | - | - | - | 220 | 165 |
| Ag nanoparticle (island), photonic crystal | Ag | 350-1100 | - | - | - | 60 (broadband) | 60 | 163 |
| Au island film | Au | 570 | 12 | 5 | - | - | 12 | 147 |
| Au/Ag NP | | | | | | | | |
| Au nanoparticle | Au | 540 | - | - | 49.8 | 109 (345 nm) | 109 | 65 |
| Au nanosphere | Au | 550 | - | - | 21 | 76 (275 nm) | 76 | 150 |
| Au nanorod | Au | 520, 805 | 6 | - | 6 | 27 (805 nm) | 27 | 141 |
| Ag nanoparticle | Ag | 400 | 14.4 | 12.2 | - | - | 14.4 | 60 |
| Ag nanoparticle | Ag | 420 | 10 | 11 | - | - | 11 | 116 |
| Au/Ag NP array | | | | | | | | |
| Au, Ag nanoparticle array | Au | 550 | 5.2 | 3.5 | - | - | 45 | 139 |
| Au, Ag nanoparticle array | Ag | 420 | 30 | 45 | - | - | 45 | 139 |
| Au/Ag core-shell | | | | | | | | |
| Ag nanosphere core | Ag | 530 | 40 | 30 | - | - | 40 | 161 |
| Ag nanosphere core | Ag | 400-1000 | - | - | - | 40 (white) | 40 | 172 |
| Au, Ag nanoparticle core | Au, Ag | 420, 510 | 21 (Au) | - | 20 (Ag) | - | 21 | 171 |
| Au/Ag glass composite | | | | | | | | |
| Au nanoparticle | Au | 630 | 4.8 | 30 | - | - | 30 | 123 |
| Ag nanoparticle | Ag | 522 | 4.5 | 10.6 | 16.6 | - | 16.6 | 138 |
| Au-antimony nanoparticle | Au | 632 | 10.7 | 8 | - | - | 10.7 | 126 |

Table 1. Upconversion enhancement factors for various emission lines, materials and geometry used for plasmon enhancement. The entries are selected from Figure 6 for those reporting enhancements greater than 10.

3.1 Plasmon Enhancement of Excitation Process

First, the plasmonic structures used for upconversion enhancement can largely be classified into two types: plasmon resonance at emission or excitation wavelengths. As discussed in detail in the previous section, the plasmons resonant with emission band enhance the

upconverted luminescence by the Purcell effect while the plasmon resonance at the excitation wavelength enhances absorption and energy transfer processes as well as the detrimental increase of infrared emission rate. In both cases, metal presents nonradiative decay channels leading to quenching. The Purcell enhancement of upconverted luminescence would not make a dramatic enhancement while the excitation enhancement can be very large especially in the weak excitation limit thanks in large part to the quadratic dependence on the absorption enhancement. The realization that the plasmon matched to the excitation wavelength has much greater potential for enhancement is relatively new and there are only a few papers on them, most of which were published within the last few years. The largest enhancement for the Yb-Er upconversion system was reported with an array of disk-coupled dot on pillar, a two layer structure composed of gold dots coated on top of nanopillars and suspended over holes on a gold film. This structure exhibited a plasmon resonance near 980 nm when the pillar height was properly adjusted. Under a weak excitation with 400 W/cm^2 or lower, the green and red emission was enhanced by 310x and 100x, respectively, compared to the reference sample on a glass substrate.⁶¹ It is interesting to note that a pillar height resulting in an apparently strong plasmon resonance at 980 nm yielded a lower upconversion enhancement. This may be attributed to stronger absorption of the excitation light and also more severe quenching in this geometry. In fact, the decay of the visible luminescence was found to be shortened by a factor of 8, a significant fraction of which may have been due to nonradiative decay. Other structures including pillar,⁶³ hole⁵⁸ and pyramid⁹⁰ arrays have also been tuned to match the plasmon resonance to the excitation wavelength, yielding enhancement factors between 3 and 68. Unfortunately, none of these papers specified the exact excitation power densities but, based on the relatively large enhancement factors, 33x and 68x, reported for the hole and pyramid arrays, respectively, we speculate the measurements

were done in the weak excitation regime. For the pillar array, the green emission intensity showed a $P^{1.55}$ dependence on the pump power, P , suggesting that the excitation power was in the intermediate region between the weak and strong excitation limits. Therefore the saturation of intermediate level must have begun to occur, which partially explains the low enhancement factor of 3. The same group also reported an enhancement of Yb-Tm upconversion by up to a factor of 5 using the same gold pillar array.¹¹⁶ The excitation power density was $\sim 100 \text{ kW/cm}^2$, suggesting that the measurements were done in the strong excitation regime and thus the observed enhancement was mostly due to absorption enhancement. The modest enhancement factors between 1.5 and 5.5 reported in this work are consistent with the typical absorption enhancement achieved with gold nanopillars.

We note that all of the above-mentioned studies dealt with periodic structures. In contrast to isolated or randomly distributed plasmonic nanostructures supporting localized surface plasmon, periodic structures exhibit well defined coupling conditions for the incoming light imposed by the periodicity. This coupling condition gives rise to unique angular and wavelength dependence. Verhagen et al. studied Er^{3+} upconversion enhancement by a square array of square holes on a gold film fabricated on a sapphire substrate implanted with Er^{3+} ions.¹¹⁷ This system exhibits extraordinary transmission in which coupling with surface plasmon polariton mode results in strongly enhanced transmission through subwavelength scale holes.¹¹⁸ The periodic hole array acts as a grating coupler providing to the incoming light an additional tangential momentum needed to couple to the surface plasmon polariton mode. Therefore, the resonance frequency and local field enhancement are jointly determined by the periodicity and the hole size and shape. Verhagen et al. adjusted the periodicity so that the structure exhibited extraordinary transmission at 1480 nm and consequently excited the Er^{3+} ions implanted in the sapphire

substrate, inducing upconverted luminescence at 550, 660, 810 and 980 nm via four-, three- and two-photon upconversion processes. They then adjusted the hole size for maximum field enhancement and consequently upconversion enhancement, which was 450x at the pump power density of 2 W/cm². It is noted that Er³⁺ ions under 1480 nm excitation exhibit both ETU and ESA and thus the exact dynamics of upconversion is highly complex. The limiting behaviors in the weak and strong excitation limits, however, remain the same. For the two-photon upconversion to 980 nm emission, the pump intensity dependence is quadratic in the weak excitation limit and linear in the strong excitation limit. We thus anticipate the enhancement factors would go as F_a^2 and F_a in the weak and strong excitation limits, respectively, as in the pure ETU process. The enhanced absorption due to the local field enhancement should account for a large fraction of the observed enhancement with some contribution also from the enhancement of energy transfer process. In addition to the simple square holes, annular apertures were also studied. Periodic arrays of annular apertures may support surface plasmon polariton or localized surface plasmon, depending on the aperture size. Small apertures support surface plasmon polariton with sharp transmission resonance while large apertures exhibit localized surface plasmon with broad transmission band. The small aperture with surface plasmon polariton yielded a very large upconversion enhancement of 370x, comparable to the square hole array, while the large aperture with localized surface plasmon gave only 10x enhancement. This indicates that surface plasmon polariton gave a greater field enhancement than localized surface plasmon. The only other study that has dealt with localized surface plasmon for excitation enhancement is the one by Greybush et al. who coupled NaYF₄:Yb³⁺,Er³⁺ upconversion nanoparticles with gold nanorods.¹¹⁹ In this work, the plasmon enhancement was clearly shown by the distinct polarization dependence and a modest enhancement of ~2x was observed. The

small enhancement is partly due to the high pump power density of $10^5 \sim 10^6$ W/cm², which puts them in the strong excitation limit and thus the overall upconversion enhancement is due entirely to absorption enhancement. At lower pump power densities, the enhancement factor should increase. However, it appears unlikely the enhancement factor could increase to several hundred and become comparable to the surface plasmon polariton cases. Therefore, although the local field enhancement depends on the details of the nanostructure design, it might be taken as a general trend that surface plasmon polariton is more advantageous for upconversion enhancement than localized surface plasmon.

3.2 Plasmon Enhancement of Emission

The vast majority of papers reporting plasmon enhanced upconversion chose plasmon resonance matched to the emission wavelengths using novel metal nanoparticles. A simple and thus popular technique to place lanthanide ions in the vicinity of metal nanoparticles is to prepare a lanthanide doped glass containing metal nanoparticles. Doped glass materials are typically prepared by the standard melt technique and metal nanoparticles are either directly added to the precursor melt or formed by reducing metal ions during the annealing or quenching process. In most cases, gold or silver nanoparticles were used. Gold nanoparticles resulted in upconversion enhancement mostly between 2 and 30.¹²⁰⁻¹²³ Silver nanoparticles produced enhancement ranging from 1.35 to 17.¹²⁴⁻¹³⁵ The upconverted luminescence intensity generally increases with increasing metal nanoparticle concentration until it reaches a maximum and begins to decrease as quenching dominates over enhancement. The enhancement is typically attributed to the effect of surface plasmon. Since the lanthanide ions are uniformly doped and the metal nanoparticles are relatively sparsely dispersed, the observed enhancement is an averaged value over many ions

located at various distances from metal nanoparticles. Also, there appear to be other effects in play as well in some cases. Gold nanoparticles dispersed in a glass host exhibit plasmon resonance in the red spectrum and therefore the red emission band is enhanced more than the green emission band thanks to the better spectral overlap.¹²⁰ When the particle sizes are in 4-6 nm range, however, they do not show distinct plasmon peak because the plasmon resonance is strongly damped due to the increased surface scattering of electrons.¹³⁶ Even in such cases, enhanced upconversion has been observed.^{122,123} In these cases, however, it is difficult to attribute the enhanced upconversion to plasmon enhancement. Instead, enhanced light scattering by the small gold nanoparticles may be the origin of the observed enhancement. Uniform enhancement over a broad range of spectrum from green to infrared is consistent with this conjecture. It may also be noted that most papers report modest enhancement between 2 and 7 while in one case 30x enhancement was reported for the red emission.¹²³ In this work, 6 nm gold nanoparticles were used and the local field enhancement was estimated to be 2~3. The large observed enhancement is thus unlikely due entirely to plasmon effect.

In the visible frequency region, silver exhibits much less intrinsic loss than gold and is therefore better suited for plasmon enhancement.¹³⁷ Naturally, one can find many more papers reporting silver nanoparticles dispersed in glass hosts than gold. Silver nanoparticles generally produce plasmon peaks in the blue region between 450 nm and 500 nm and thus do not provide good spectral overlap with the upconverted green and red luminescence of Er^{3+} ions. Despite the spectral mismatch, many papers reported enhancement of green and red emission of Er^{3+} . The large off-resonance enhancement raises the possibility that increased light scattering by the metal nanoparticles is at least partially responsible for the observed enhancement. Considering the spectral overlap, good enhancement is expected for the blue emission excited by the three-photon

process in the Yb^{3+} - Tm^{3+} system which to our knowledge has not been done yet. Instead, it has been reported that the blue emission arising from the excited state absorption of Nd^{3+} ion was enhanced by a factor of 17.¹³⁸ In this case, however, the plasmon resonance was observed at 522 nm, suggesting some clustering of silver nanoparticles. It was also observed that the green emission at 527 nm was enhanced only by 4.7 despite better spectral overlap. It is thus unclear how much of the observed enhancement was due to plasmon.

While glass is an attractive host for certain applications such as windows and coatings, the inherently disordered structure makes it difficult to quantitatively determine the effect of surface plasmon. Also, the high density of defects tends to lower the quantum efficiency. Furthermore, most glasses are oxides with large phonon energies and thus exhibit significant nonradiative transition rates. An alternative approach is to couple upconversion nanoparticles or nanorods with gold nanoparticles. This may be accomplished by physically or chemically conjugating upconversion nanoparticles with gold nanoparticles or coating gold nanoparticles with upconversion material.^{62,65-67,69,139-152} Enhancement factors vary widely. For the Yb^{3+} - Er^{3+} system, the reported values for green emission enhancement ranges from 72% decrease to 10x enhancement. A commonly adopted morphology is to decorate gold nanoparticles on the surface of upconversion nanoparticles. It is interesting to note that in this system enhanced upconversion was observed only for upconversion nanoparticles with sizes greater than 90 nm.^{62,65,66,141,144,145,148,150,152} When the upconversion nanoparticle sizes were between 10 nm and 80 nm, they exhibited quenching.^{69,140,143,146} We do not suggest there exists a hard boundary between enhancement and quenching but the clear division of enhancement and quenching based on upconversion nanoparticle size in the gold nanoparticle decorated upconversion nanoparticles does reveal the interplay between plasmonic enhancement and quenching by metal. As shown in

Figure 3, quenching is generally dominant at very short distances while the plasmon enhancement effect has a farther reach. From this perspective, the observed size dependence can easily be understood. When the upconversion nanoparticle is small, all lanthanide ions are located at distances where quenching dominates. For large nanoparticles, there are more lanthanide ions farther away from the metal surface and thus more plasmon enhancement and less quenching. The notion of optimal distance from the metal surface for maximum enhancement is a universal theme in any plasmonic nanostructures involving luminescent ions or molecules.¹⁵³ It is common to incorporate a spacer layer to provide sufficient distance between optically active ions and metal surface so that quenching is alleviated. This has been done in a wide range of nanostructures including nanoparticles, nanorods, core-shells, nanoparticle films, and nanopatterned films. The role of spacer layer is further discussed later.

One of the fundamental difficulties in the systems involving metal and upconversion nanoparticles is to precisely control the local environment of the lanthanide ions. In most cases the coupling between gold and upconversion nanoparticles is conducted by a solution-based process. There is inevitably a wide variation in the number of nanoparticles and more importantly the ratio of upconversion and gold nanoparticles coupled together. This is in addition to the inherent variations in the nanoparticle size and shape. It is therefore desirable to conduct experiments on a single pair of upconversion and gold nanoparticles. Schietinger et al. used an atomic force microscope to bring a single $\text{NaYF}_4:\text{Yb}^{3+},\text{Er}^{3+}$ nanoparticle to a close proximity to a single gold nanoparticle.⁶⁷ The luminescence from the upconversion nanoparticle was then collected by a confocal microscope. The green emission was enhanced by 4.8x and the red by 2.7x. Not surprisingly, the enhancement factors were sensitive to the exact arrangement of the two nanoparticles and the observed enhancement factors may not be the maximum achievable

values. Nevertheless, we may infer the higher enhancement of green is due to the better spectral overlap with the plasmon resonance of gold nanoparticle which was centered at 540 nm. Also, it was found that the upconverted emission is little influenced when the gold nanoparticle is more than 20 nm away. As the gold nanoparticle is pushed closer, the emission intensity increased first and then saturated. This was attributed to the onset of quenching and it was further supported by the continued decrease in the rise and decay times. This work provided one of the most precise and quantitative observations on the plasmon enhancement of emission and showed that the enhancement of upconverted luminescence basically exhibits the same behavior as the linear luminescence enhancement when the plasmon resonance is matched to emission wavelength.

Many attempts to enhance upconversion have been made with silver nanoparticles too.^{60,64,139,154-164} Plasmon resonance is typically in the blue but may shift to the red when the silver nanoparticles form a tight cluster and consequently exhibit plasmon hybridization. Silver nanoparticles generally offer higher local field enhancement thanks to the lower intrinsic loss than gold. Thanks to the low intrinsic loss and high field enhancement, no paper reported net quenching of upconverted luminescence when using silver nanoparticles or nanorods. Enhancement factors varied between 2 and 30. Morphology is more diverse and the comparisons are not as straightforward as the gold nanoparticle case. But silver nanoparticles seems to offer better enhancement than the gold nanoparticles and larger upconversion particles tend to exhibit higher enhancement. A very high enhancement of 220x has been observed from $\text{Al}_2\text{O}_3:\text{Er}$ films deposited on Ag islands films.¹⁶⁵ In this work, Ag islands were formed by depositing and annealing a very thin Ag film in much the same way as the common substrate for surface enhanced Raman scattering. Individual Ag island was ~220 nm in width and 50 nm in height, producing plasmon resonance centered in the red near 600 nm but stretching broadly into the

blue and infrared as well. Thus the observed enhancement should contain both the excitation and emission enhancement. When the Ag island size was reduced to 100 nm in width and 15 nm in height, the plasmon peak narrowed significantly and exhibited a well-defined peak centered at 480 nm with almost no absorption in the infrared. In this case, the upconversion enhancement was only 2.5, which may be taken as the emission enhancement factor. Then, from the total enhancement of 220x, the enhancement factor for the excitation process may be calculated to be ~90x. If we assume the upconversion is entirely due to ESA and weak excitation condition was used (the pump power density was not given in this paper), then we deduce absorption enhancement of ~9x. Accounting for the luminescence quenching by silver, the actual enhancement should be higher, while the contribution by energy transfer upconversion and the possible enhancement of energy transfer rate by plasmon would decrease the actual absorption enhancement. In any case, an absorption enhancement factor of around 10 is within the range commonly observed in silver nanostructures. A similar approach has been made with Au island film deposited by sputtering on top of a high density NaYF₄:Yb,Er upconversion nanoparticle film prepared by Langmuir-Blodgett method.¹⁴⁷ Under 980 nm excitation, the emission intensities for 522, 550 and 652 nm were enhanced by factors of 12, 5 and 5, respectively. The intensities showed nonlinear dependence on excitation power density in the weak excitation regime and the enhancement factor peaked at the transition point between weak and strong excitation regimes. The higher enhancement factor for 522 nm emission is likely due to the significant contribution by three-photon upconversion process, as indicated by the nearly cubic power dependence. It is also possible local heating contributed to the preferential increase of 522 nm peak. The enhancement factors were overall lower than the Ag island film, which is likely due to the higher intrinsic loss in gold. The large enhancement factors observed in the metal

island films, especially in the Ag island film, reinforces the fact that the metal island films are effective in creating hot spots where the local field is highly enhanced. However, these films generally produce highly non-uniform structures where the field enhancement is extremely sensitive to position and thus difficult to control.

One approach to gain better control over the local environment of the lanthanide ions is to use a core-shell structure. In addition to the more uniform geometry, metal nanoshells allow wide tuning of plasmon resonance, providing additional degrees of freedom.¹⁶⁶⁻¹⁶⁸ Gold nanoshells have been used with NaYF₄:Yb,Er and NaYF₄:Yb,Er,Tm cores. The enhancement factor is strongly dependent on the shell geometry and the plasmon resonance position. When the plasmon resonance is located within the wavelength range between 580 nm and 820 nm, the upconverted luminescence was quenched.^{66,169,170} When the plasmon resonance was matched to the excitation wavelength of 980 nm, enhanced upconversion was observed.¹⁷⁰ Gold and silver nanoshells grown on a triply doped NaYF₄:Yb,Er,Tm nanoparticles resulted in a ~3x and ~20x enhancement for the green and blue-violet emission, respectively.¹⁷¹ Gold nanoshell exhibiting plasmon resonance in the green preferentially enhanced green emission while silver nanoshell with plasmon peak in the blue selectively enhanced blue-violet emission. It is not immediately clear why one system exhibited quenching for emission matched nanoshell plasmon resonance while another system showed enhancement. One complication with the metal nanoshell on upconversion nanoparticle core is that both the excitation light and emitted luminescence have to go through the metal shell, which attenuates light. It seems thus better to have a metal core and upconversion material shell. Growing a high quality upconversion material shell on a metal nanoparticle is extremely challenging. Uniform shell morphology requires amorphous material but high luminescence efficiency prefers high crystallinity. It is thus necessary to find a

polycrystalline shell whose grain sizes are large enough to ensure good luminescence efficiency yet small enough to form uniform shell. Er-doped or Yb,Er co-doped oxide shells have been made on silver or gold nanoparticle cores.^{149,156,161} All oxide core-shell structures involved SiO₂ spacer layers between metal core and oxide shell to alleviate quenching and exhibited upconversion enhancement factors of 5 ~ 10. In the cases of Ag-Y₂O₃:Er³⁺, Au-Y₂O₃:Yb³⁺,Er³⁺ and Ag-Lu₂O₃:Gd/Yb/Er core-shell structures, the green emission was preferentially enhanced more than the red emission.^{149,156,161} This is most likely due to the better spectral overlap with the nanoparticle plasmon resonance which was located in the blue-green region. Recently, plasmon enhancement of upconversion in Ag-SiO₂-Er₂O₃ core-shell structure has been reported.¹⁷² Er₂O₃ has not been studied for upconversion or even for linear luminescence because Er is known to exhibit severe quenching at high concentrations due to cross-relaxation. Er₂O₃ however was found to exhibit broadband emission at high excitation power densities, indicating a departure from the characteristic lanthanide optical transitions. It was found that broadband emission occurred when the temperature reached 450 K and the authors attributed the broadband emission to thermal generation of holes in the valence band and subsequent recombination of electrons in the defect states with valence band holes. The enhancement factor reached as high as 10⁴. There is only one paper reporting fluoride (NaYF₄:Yb³⁺,Er³⁺/Ho³⁺) shell on metal (gold) nanoparticle core, presumably due to the difficulty in synthesis.¹⁵¹ This system exhibited quenching of green emission while the red emission remained almost unchanged. This was attributed to the resonant quenching by the gold nanoparticle surface plasmon and was supported by the photothermal effect data, which showed more effective heating with the core-shell structure than with the gold nanoparticle only. Inserting a spacer layer between the metal core and the upconversion shell should alleviate quenching and possibly lead to enhancement of

upconversion. The spacer layer could simply be an undoped fluoride shell, which could presumably be synthesized with a procedure to the upconversion shell. Recently, NaYF₄:Yb³⁺,Er³⁺ nanoparticles with doped and undoped shells have been demonstrated²⁷ and this procedure may be extended to synthesize undoped spacer layer in a metal-upconversion core-shell structure.

An alternative approach to achieve more uniform local environment for the upconversion materials is to create regular arrays of nanoparticles. Metal and dielectric nanoparticles can be arranged into periodic structures by self-assembly. At least two groups have reported self-assembled upconversion nanoparticles deposited on top of self-assembled gold and silver nanoparticle layers. Xu et al. reported a layer-by-layer deposition of silver nanoparticles and upconversion nanoparticles by the solve evaporation method.¹⁵⁴ Due to the coupling of plasmon resonances, the silver nanoparticle film exhibited a very broad absorption band extending from 400 nm to 1000 nm. Under high energy excitation, the red and green Er³⁺ luminescence showed little enhancement while it was enhanced by ~3x under 980 nm excitation. The enhancement was thus attributed to the excitation enhancement by the significantly broadened plasmon resonance. Any emission enhancement by the visible plasmon must have been canceled by quenching. Saboktakin et al. used spin-coating to prepare a regular array of gold and silver nanoparticles.¹³⁹ Atomic layer deposition was then used to deposit Al₂O₃ spacer layer on which NaYF₄:Yb³⁺,Er³⁺ and NaYF₄:Yb³⁺,Tm³⁺ upconversion nanoparticle layer was formed by interfacial self-assembly and monolayer transfer. The gold and silver nanoparticle films exhibited narrow and well-defined plasmon peaks only slightly shifted from the signatures of colloidal particles, indicating that the nanoparticles are not densely packed in the nanoparticle films. The enhancement factors were found to be highly sensitive to the spacer layer thickness. The 5 nm thick Al₂O₃ layer

yielded the highest enhancement for gold nanoparticle film while 10 nm gave the highest enhancement for silver nanoparticle films. The maximum enhancement was $\sim 5x$ with the gold nanoparticles and $\sim 45x$ with the silver nanoparticle film, both of which were obtained with the green upconverted emission of $\text{NaYF}_4:\text{Yb}^{3+},\text{Er}^{3+}$. It may seem counterintuitive gold exhibited a smaller optimum thickness than silver for the spacer layer despite the higher intrinsic loss and thus stronger quenching. However, it should be kept in mind that the optimum spacer layer thickness is determined by the interplay between quenching and plasmon enhancement. The higher intrinsic loss leads not only to stronger quenching but also to weaker plasmon resonance. Thus the combination of the two could result in a smaller optimum spacer layer thickness and this is consistent with the smaller enhancement factors observed for the gold nanoparticle films.

The interplay between field enhancement, spontaneous emission enhancement and nonradiative transition enhancement can be quantitatively determined by the expressions we derived in the previous section. Since the various effects are highly sensitive to the precise geometry of the plasmonic nanostructures, the net effect of surface plasmon on the optical transitions is in principle accurately determined only by full numerical calculations. Simplified models that could provide intuitive understanding would be helpful. In a simple model, the nonradiative transition induced by the presence of metal may be described by Förster energy transfer process between the optically active ion modeled as a dipole and the acceptor dipoles in metal.¹⁰⁰ In this case, the R^{-6} dependence of dipole-dipole energy transfer rate given by the Förster theory yields a d^{-3} dependence after integration over all acceptors distributed in the three-dimensional volume of metal, where d is the distance between the metal surface and the optically active ion. To extend this theory to a monolayer of metal nanoparticles, we consider the Förster energy transfer rate between a metal nanoparticle and an optically active ion, which should

exhibit a R^{-6} dependence if the metal nanoparticle is small enough and thus can be regarded as a pure dipole. Integrating over the two-dimensional array of metal nanoparticles then yields a d^{-4} dependence.^{115,173} A two-dimensional array of metal nanoparticles or a thin metal film should thus require a smaller spacer layer thickness in general than three-dimensional arrays of metal nanoparticles or bulk metal, although the optimal thickness will be determined by the actual transfer rate which depends also on spectral overlap and dielectric environment among other things. It is straightforward to extend this argument to a linear chain of metal nanoparticles or a metal nanowire to obtain a d^{-5} dependence while a pair of single nanoparticle and single upconversion nanoparticle would retain the original d^{-6} dependence from the Förster theory. These distance dependences of nonradiative transition rates would compete against the enhanced radiative decay rates by the Purcell effect to determine the optimal spacer layer thickness.

3.3 Plasmonic Effect on Upconversion Dynamics and Local Heating

So far we have only discussed the upconverted luminescence intensities but examining the transient behavior would shed light on the dynamics of the upconversion process. Solving the rate equations to get the exact time dependence is difficult. Instead we may try to get a simplified solution for time evolution of green luminescence. To do this, we first rewrite equation (10) as

$$\frac{dN_{A4}}{dt} = c_{d4} N_{D1} N_{A2} - W_{A4} N_{A4} \quad (37)$$

where $W_{A4} = W_{A40} + W_{A43}$. Denoting the first term in the right hand side as $f(t)$, we can find a general solution as,

$$N_{A4}(t) = \exp(-W_{A4}t) \int \exp(W_{A4}t) f(t) dt \quad (38)$$

Since we don't know the exact functional form of $f(t)$ until we fully solve the rate equations, we assume a simple exponential form and examine the rise and decay of the upconverted luminescence at the leading and trailing edges of an excitation pulse. For rise, we assume

$$f(t) = A(1 - \exp[-W_{DR}t]) \quad (39)$$

where W_{DR} is the rate constant describing the rise of the intermediate energy level population, $N_{D1}N_{A2}$, and A is a constant. The time evolution of the emitting level population, N_{A4} , is then given as,

$$N_{A4}(t) = \frac{A}{W_{A4}} - \frac{A}{W_{A4} - W_{DR}} \left(\exp[-W_{DR}t] - \frac{W_{DR}}{W_{A4}} \exp[-W_{A4}t] \right) \quad (40)$$

Equation (40) appears to have singularity when $W_{A4} = W_{DR}$ but in that case N_{A4} simply exhibits single exponential decay. The above equation shows that the rise of the upconverted luminescence is governed by the competition of two competing rates, W_{DR} and W_{A4} , which describe the excitation rate of the intermediate levels and the decay of the emitting level. If one of the two rates is much greater than the other, the rise is dominated by the slower of the two. If the two rates are comparable, the initial rise should be slow, increasing as t^2 . At longer times, the rise will become exponential with the rate constant equaling the slower of the two. Decay can be described similarly. This time, we assume

$$f(t) = A \exp[-W_{DD}t] \quad (41)$$

where W_{DD} represents the decay rate for the intermediate level population, $N_{D1}N_{A2}$, and A is a constant. The decay of the emitting level population, N_{A4} , can now be written as,

$$N_{A4}(t) = \frac{A}{W_{A4} - W_{DD}} \left(\exp[-W_{DD}t] - \frac{W_{DD}}{W_{A4}} \exp[-W_{A4}t] \right) \quad (42)$$

Once again, time evolution of the upconverted luminescence is determined by two competing exponential functions characterized by a slow initial decay followed by exponential decay with rate constant equaling the slower of the two. When the two rate constants are very different, the decay appears single exponential with the slower rate constant. And the decay becomes truly single exponential when the two rates are equal to each other. In the Yb-Er upconversion system, the intermediate energy levels of $^2F_{5/2}$ and $^4I_{11/2}$ of Yb^{3+} and Er^{3+} , respectively, are known to have long lifetimes on the order of 1 ms while the emitting level, $^4S_{3/2}$ of Er^{3+} , has a shorter lifetime in the range of 100 μs .^{4,174} The actual excitation and decay rates, W_{DR} and W_{DD} , in upconversion material contain both the decay and upconversion rates and should therefore be faster than these intrinsic decay rates. We have not been able to find any work that measured or estimated W_{DR} or W_{DD} , and thus cannot determine how the rates might change. In any case, it should be noted that the apparent decay rate measured by time-resolved photoluminescence spectroscopy might be the decay of the intermediate energy levels rather than the emitting level.

Surface plasmon can change all three rate constants, W_{A4} , W_{DR} and W_{DD} . The possible changes in W_{A4} have been described earlier. It is important note that the anticipated increase in W_{A4} by the plasmonic effect does not necessarily mean the observed decay rate of upconverted luminescence should increase. If the decay rate of the intermediate level, W_{DD} , is slower than W_{A4} , W_{DD} will determine the actual decay. W_{DD} can be influenced by surface plasmon, especially when the surface plasmon resonance is matched to the excitation wavelength, which is close to the emission wavelength of the intermediate levels. How surface plasmon modifies W_{DD} should be the same as the way W_{A4} is changed. Therefore, despite the fact that any decrease in observed decay time is often attributed to the increased W_{A4} without justification, it might actually be due to the changes in the decay rate of the intermediate levels, W_{DD} , for the reasons

stated above. Similarly, it should be kept in mind that the rise is determined by both the decay rate, W_{A4} , and the excitation rate, W_{DR} . Thus, it is possible that an increase of W_{A4} by, for example, the Purcell effect can increase the rise rate of the upconverted luminescence, if the excitation rate is faster. If W_{A4} is faster than W_{DD} , the rise is determined mainly by W_{DD} and any changes in W_{A4} does not influence the rise time. Almost all papers which studied either rise or decay of the upconverted luminescence report enhancement of both decay and rise rates by plasmonic nanostructures. Among the studies with emission matched plasmon resonances, many reported faster decay of the upconverted luminescence^{66,67,140,148,149,154,156,158,161,169} while two reported no change.^{128,175} Since the plasmon is matched to the emission wavelength, we can anticipate Purcell enhancement for the upconverted luminescence and also increased nonradiative decay for both the emitting level and the intermediate levels. The measured decay times of the upconverted luminescence ranged from 20 μ s to 300 μ s. The reduction of decay time due to plasmon varied between 25% to 200% among the works that reported decay time reduction. All papers that reported reduced decay time attributed it to the faster decay of the emitting level, which is W_{A4} in our notation. We caution however that the apparent decay of the upconverted luminescence might actually represent the decay of the intermediate energy level. It would be instructive to measure the luminescence decay in the infrared region to probe the intermediate level dynamics directly but this has yet to be done. Among the studies that used excitation matched plasmon resonance, the measured decay times varied between 16 and 300 μ s with plasmonic nanostructures.^{58,61,116} The reduction in decay time due to plasmonic nanostructure was in the range of 16% ~ 87%. In the case of excitation matched plasmonic nanostructures, the plasmon would influence both the radiative and nonradiative decay rates of the intermediate levels and also introduce additional nonradiative decay rate to the emitting level.

Since the intermediate level decay is expected to be affected more severely, there is generally a greater chance the measured decay of the upconverted luminescence actually represents the decay of the emitting level but any conclusive experiments probing both the visible and infrared luminescence decays have yet to be done. Recently, the infrared decay of $\text{NaYF}_4:\text{Yb}^{3+},\text{Er}^{3+}$ nanoparticles on silver nanograting was reported.⁹³ The infrared decay time was measured to be 200 μs , more than 8 times faster than the decay of the same samples deposited on glass. The nanograting used in this work offered only a small Purcell factor and the measured decay times were roughly the same for both nanograting and flat silver film. Thus the observed reduction in decay time was attributed to the nonradiative decay introduced by the metal surface. It should be noted that the measured decay time should include not only the radiative and nonradiative decay rates but also the upconversion rate. This work therefore allows an indirect inference to the energy transfer upconversion rate, although a more comprehensive work should be done for any definitive conclusion. The rise time complements the decay time data and provides more complete information about the upconversion process. An increase in rise time has been reported in a single pair of gold nanoparticle and $\text{NaYF}_4:\text{Yb}^{3+},\text{Er}^{3+}$ upconversion nanoparticle.⁶⁷ The green rise time was reduced from 50 to 20 μs while the red showed a larger reduction from 85 to 35 μs . Also, a 40% faster rise of green luminescence was observed from the $\text{NaYF}_4:\text{Yb}^{3+},\text{Er}^{3+}$ upconversion nanoparticles deposited on a nanohole array fabricated in a gold film.⁵⁸ The faster rise is usually attributed to more efficient upconversion. This may well be true but the interplay between W_{DR} and W_{A4} must be carefully considered. A more comprehensive study under various experimental conditions is needed to build a full picture on the upconversion dynamics and how plasmons affect them.

The last topic we discuss is the effect of heating which in many cases is inevitable due to the absorption by metal. Temperature is a universal factor that affects all types of optical transitions. In general, temperature dependence of luminescence arises from the competition between radiative and nonradiative transitions. There are many nonradiative transition mechanisms that can affect luminescence but the multiphonon emission in which the excited electronic state relaxes to a lower energy state by emitting phonons is the most relevant process for optically active ions and molecules. For lanthanide ions, the $4f$ electronic states are well shielded from the crystalline environment by the outer shell electrons and thus the electron-phonon coupling is generally weak. In this weak coupling regime, multiphonon emission rate is given by,¹⁷⁶

$$W_{MPE}(T) = W_{MPE}(0)(n+1)^p \quad (43)$$

where n is the phonon occupation number given by the Bose-Einstein statistics and $p = \Delta E/h\nu$ is the number of phonons with energy, $h\nu$, required to bridge the transition energy, ΔE . In general, equation (43) describes the temperature dependence quite well but the precise determination of $W_{MPE}(0)$ is difficult. $W_{MPE}(0)$ is typically determined experimentally by measuring nonradiative transition rates at various temperatures and extrapolating to $T = 0$ K. The modified energy gap law proposed by van Dijk and Schuurmans is commonly used for $W_{MPE}(0)$,¹⁷⁷

$$W_{MPE}(0) = \beta \exp\left[-(\Delta E - 2h\nu_{\max})\alpha\right] \quad (44)$$

where ν_{\max} is the highest vibrational frequency and α and β are constants. Equation (43) predicts increasing multiphonon emission rate with increasing temperature, which consequently leads to decreasing luminescence intensity. This universal phenomenon is called thermal quenching.

When upconversion material is coupled to a metallic nanostructure, light absorption by metal increases the local temperature and the local heating can be greatly amplified when the excitation is matched to plasmon resonance. The local heating can be used for sensing and medical applications^{143,170,178-180} but heating tends to decrease the upconversion efficiency by thermal quenching.^{181,182} In the case of Ag-SiO₂-Er₂O₃ core-shell structure, the presence of Ag nanoparticle increased the temperature by 100 °C compared to the Er₂O₃ nanoparticles under the same excitation condition.¹⁷² Such a large temperature increase could lead to severe thermal quenching, negating any plasmonic enhancement effect. Thermal quenching cannot be entirely avoided but may be alleviated when the host material has small phonon energies. In this sense, fluoride hosts are generally favored to oxides. The Yb-Er upconversion system provides a good indicator for the crystal temperature. In this system, the green upconverted luminescence is composed of two closely spaced lines at 525 and 545 nm which originate from ²H_{11/2} and ⁴S_{3/2} levels, respectively. Since the two energy levels are closely spaced, their occupation is governed mainly by the thermal distribution according to the Boltzmann factor,

$$\frac{N_H}{N_S} = \alpha \exp\left[-\frac{\Delta E_{HS}}{kT}\right] \quad (45)$$

where N_H and N_S are the population of ²H_{11/2} and ⁴S_{3/2} levels, respectively, ΔE_{HS} is the gap between the two levels and α is a constant. The intensity ratio of the two lines can then be written as,¹⁸²

$$\frac{I_H}{I_S} = \frac{N_H}{N_S} \frac{W_{HR}(W_{SR} + W_{SNR})}{W_{SR}(W_{HR} + W_{HNR})} \quad (46)$$

Here W_{HR}, W_{HNR}, W_{SR} and W_{SNR} are radiative and nonradiative decay rates for the ²H_{11/2} and ⁴S_{3/2} levels, respectively. The nonradiative decay rates are described by the multiphonon

emission rate given in equation (43). Since the difference in energies of the two $^2H_{11/2}$ and $^4S_{3/2}$ levels is much smaller than the transition energies, we may assume the nonradiative decay from the $^2H_{11/2}$ level should be dominated by the decay to the lower lying $^4S_{3/2}$ level and thus,

$$W_{HNR}(T) = W_{HNR}(0)(n+1)^{\Delta E_{HS}/h\nu} \quad (47)$$

Furthermore, W_{SNR} may be considered temperature independence as the next lower lying energy level $^4F_{9/2}$ is far below the $^4S_{3/2}$ level. One may then arrive an expression describing the temperature dependence of the intensity ratio between the two green emission lines as below.

$$\frac{I_H}{I_S} = \frac{\beta \exp(-\Delta E_{HS}/kT)}{1 + \gamma [1 - \exp(-h\nu/kT)]^{-\Delta E_{HS}/h\nu}} \quad (48)$$

where $\beta = \alpha(1 + W_{SNR}/W_{SR})$ and $\gamma = 1 + W_{HNR}/W_{HR}$. Equation (48) predicts the intensity ratio should increase with increasing temperature up to a certain temperature and then decrease after reaching a peak. Experiments on $Y_2O_3:Yb^{3+},Er^{3+}$ and $NaYF_4:Yb^{3+},Er^{3+}$ nanoparticles showed that the intensity ratio monotonically increased within the measurement range, which was up to 600 K for $Y_2O_3:Yb^{3+},Er^{3+}$ and 430 K for $NaYF_4:Yb^{3+},Er^{3+}$.^{181,182} This behavior allows for a convenient real-time determination of temperature simply by monitoring the intensity ratio.

4. Summary and Outlook

Recent years have witnessed an explosive growth in research on plasmon enhancement of upconversion. Although the luminescence upconversion has a long history of research and development, the recent marriage with nanophotonics, especially plasmonics, opens a wide array of new opportunities for both fundamental scientific research and developing novel applications. The plasmon enhanced upconversion is gathering interests from both the materials research community and the photonics community as it offers a new way to engineer the optical processes

and enhance efficiencies for the traditional upconversion materials while at the same time presents a less explored nonlinear optical process to the nanophotonics community which is paying attention increasingly to nonlinear optics.¹⁸³ The large and expanding body of theoretical and experimental studies is rapidly uncovering the mechanisms with which the nanophotonics environment influences various optical processes including luminescence, energy transfer, absorption and nonradiative decays. The highly complex nature of the upconversion process however awaits further elucidation. The complete understanding of the complex dynamics of upconversion under plasmonic fields could enable rational design of plasmon enhanced upconversion and consequently pave the road to new applications.

Among the potential applications of upconversion materials, solar cell and biomedical imaging have received most attention. Solar energy conversion with photovoltaic devices suffers from two major loss pathways. First, photons with energy less than the bandgap of the absorber are not absorbed and thus wasted. High energy photons create electron-hole pairs with excess energy, $E_{\text{photon}} - E_{\text{bandgap}}$, which is eventually lost by thermalization. These processes limit the efficiency of a single junction solar cell to the so-called Shockley-Queisser limit, which is 33.7% for a bandgap of 1.4 eV and 31% for silicon.¹⁸⁴ The Shockley-Queisser limit may be exceeded if efficient frequency conversion mechanisms are incorporated to enable below-bandgap absorption and avoid thermalization loss of high energy photons. Trupke et al. estimated that upconversion can increase the limiting efficiency to 50.7% for a bandgap of 2.0 eV and 40.2% for silicon.¹⁸⁵ For silicon solar cell, Er^{3+} -activated upconverter is used to upconvert 1500 nm light while amorphous silicon and other larger bandgap materials can use Yb-Er or Yb-Tm upconverters for 980 nm absorption.^{186,187} The increase in photocurrent and external quantum efficiency has been demonstrated but in order to have a real impact on the mainstream photovoltaic technology the

upconversion efficiency must be substantially increased. Plasmonic enhancement offers a promising pathway to achieve this. Another roadblock is the narrow linewidth of most lanthanide-based upconversion materials. To fully exploit the potential of upconversion, accomplishing upconversion over a broad wavelength range is critical but most lanthanide ions exhibit narrow linewidth due to the weak electron-phonon coupling in the $4f$ multiplets. Coating organic dyes can expand the absorption band.⁴⁰ Using triplet-triplet annihilation in organic materials is an alternative way to achieve broadband upconversion, although in this case it has been difficult to push the absorption band into the infrared region.¹⁸⁸ Additionally, a truly broadband upconversion by thermal radiation has recently been reported.¹⁸⁹ Coupling plasmons with these novel upconversion systems could provide an exciting way toward a viable upconversion solar cell.

Upconversion materials also have a great potential for biomedical imaging. Organic materials exhibit minimal absorption and scattering in the near infrared region. Therefore, fluorescence imaging with upconversion nanoparticle probes provide high contrast images with extremely dark background.¹⁹⁰ This is in sharp contrast to the conventional fluorescence imaging for which blue or ultraviolet light is used to excite fluorophores and typically excite strong autofluorescence in the tissue or cells. Adding plasmonic nanoparticles make multifunctional nanoparticles which can enable photothermal ablation or dark-field imaging in addition to the upconverted fluorescence imaging.^{143,170,178-180} In addition to solar cell and biomedical imaging, new applications such as sensing,⁸ security ink¹¹ and photoswitching¹² are being explored. As the theoretical understanding is being established on a firmer ground and new experimental techniques allow better control of plasmon-upconversion nanostructures, plasmon enhanced

upconversion will be an even more exciting topic of research with great potential for a wide range of applications.

Acknowledgement This work was supported in part by the National Science Foundation (CHE-1125935) and Army Research Office (W911NF-14-1-0211).

5. References

1. P. Franken, A. Hill, C. Peters, and G. Weinreich, *Phys. Rev. Lett.*, 1961, **7**, 118–119.
2. M. M. Fejer, *Phys. Today*, 1994, **47**, 25.
3. F. Auzel, *Chem. Rev.*, 2004, **104**, 139–174.
4. R. H. Page, K. I. Schaffers, P. A. Waide, J. B. Tassano, S. A. Payne, W. F. Krupke, and W. K. Bischel, *J. Opt. Soc. Am. B*, 1998, **15**, 996–1008.
5. S. Sivakumar, F. C. J. M. van Veggel, and M. Raudsepp, *J. Am. Chem. Soc.*, 2005, **127**, 12464–12465.
6. F. Wang, Y. Han, C. S. Lim, Y. Lu, J. Wang, J. Xu, H. Chen, C. Zhang, M. Hong, and X. Liu, *Nature*, 2010, **463**, 1061–1065.
7. X. Huang, S. Han, W. Huang, and X. Liu, *Chem. Soc. Rev.*, 2012, **42**, 173.
8. G. Chen, H. Qiu, P. N. Prasad, and X. Chen, *Chem. Rev.*, 2014, **114**, 5161–5214.
9. J. Zhou, Z. Liu, and F. Li, *Chem. Soc. Rev.*, 2012, **41**, 1323.
10. Q. Liu, W. Feng, T. Yang, T. Yi, and F. Li, *Nat. Protoc.*, 2013, **8**, 2033–2044.
11. J. Zhao, D. Jin, E. P. Schartner, Y. Lu, Y. Liu, A. V. Zvyagin, L. Zhang, J. M. Dawes, P. Xi, J. A. Piper, E. M. Goldys, and T. M. Monro, *Nat. Nanotech.*, 2013, **8**, 729–734.
12. L. Wang, H. Dong, Y. Li, C. Xue, L.-D. Sun, C.-H. Yan, and Q. Li, *J. Am. Chem. Soc.*, 2014, **136**, 4480–4483.
13. H. W. Leverenz, *An Introduction to Luminescence of Solids*, 1968.
14. F. Auzel, *Comptes Rendus Hebdomadaires Des Seances De L Academie Des Sciences Serie B*, 1966, **263**, 819.
15. T. Förster, *Ann. Phys.*, 1948, **2**, 55.
16. D. L. Dexter, *J. Chem. Phys.*, 1953, **21**, 836.
17. F. E. Auzel, *Proc. IEEE*, 1973, **61**, 758–786.
18. V. V. Ovsyankin and P. P. Feofilov, *Soviet Physics Uspekhi*, 1972, **15**, 354.
19. E. Nakazawa and S. Shionoya, *Phys. Rev. Lett.*, 1970, **25**, 1710.
20. J. S. Chivian, W. E. Case, and D. D. Eden, *Applied Physics Letters*, 1979, **35**, 124.
21. H. X. Mai, Y. W. Zhang, L. D. Sun, and C. H. Yan, *J. Phys. Chem. C*, 2007, **111**, 13721–13729.
22. J. D. Kingsley, *J. Appl. Phys.*, 1970, **41**, 175.
23. L. F. Johnson, *J. Appl. Phys.*, 1972, **43**, 1125.
24. Y. Mita, *J. Appl. Phys.*, 1972, **43**, 1772–1778.
25. J. C. Wright, in *Radiationless Processes in Molecules and Condensed Phases*, Springer,

- 1976, pp. 239–295.
26. X. Yu, C. J. Summers, and W. Park, *J. Appl. Phys.*, 2012, **111**, 073524.
 27. Z. Li, W. Park, G. Zorzetto, J. S. Lemaire, and C. J. Summers, *Chem. Mater.*, 2014, **26**, 1770–1778.
 28. A. Aebischer, M. Hostettler, J. Hauser, K. Krämer, T. Weber, H. U. Güdel, and H.-B. Bürgi, *Angew. Chem. Int. Ed.*, 2006, **45**, 2802–2806.
 29. E. T. Goldburt, B. Kulkarni, R. N. Bhargava, J. Taylor, and M. Libera, *J. Lumin.*, 1997, **72-74**, 190–192.
 30. K. W. Krämer, D. Biner, G. Frei, H. U. Güdel, M. P. Hehlen, and S. R. Lüthi, *Chem. Mater.*, 2004, **16**, 1244–1251.
 31. G. Yi, H. Lu, S. Zhao, Y. Ge, W. Yang, D. Chen, and L.-H. Guo, *Nano Lett.*, 2004, **4**, 2191–2196.
 32. S. Heer, K. Kömpe, H. U. Güdel, and M. Haase, *Adv. Mater.*, 2004, **16**, 2102–2105.
 33. J. H. Zeng, J. Su, Z. H. Li, R. X. Yan, and Y. D. Li, *Adv. Mater.*, 2005, **17**, 2119–2123.
 34. G.-S. Yi and G.-M. Chow, *Chem. Mater.*, 2007, **19**, 341–343.
 35. H. Schäfer, P. Ptacek, K. Kömpe, and M. Haase, *Chem. Mater.*, 2007, **19**, 1396–1400.
 36. F. Wang and X. Liu, *J. Am. Chem. Soc.*, 2008, **130**, 5642–5643.
 37. Z. Li and Y. Zhang, *Nanotechnology*, 2008, **19**, 345606.
 38. Y. Wang, L. Tu, J. Zhao, Y. Sun, X. Kong, and H. Zhang, *J. Phys. Chem. C*, 2009, **113**, 7164–7169.
 39. F. Wang, R. Deng, J. Wang, Q. Wang, Y. Han, H. Zhu, X. Chen, and X. Liu, *Nat. Mater.*, 2011, **10**, 968–973.
 40. W. Zou, C. Visser, J. A. Maduro, M. S. Pshenichnikov, and J. C. Hummelen, *Nat. Photon.*, 2012, **6**, 560–564.
 41. J. Zhao, Z. Lu, Y. Yin, C. McRae, J. A. Piper, J. M. Dawes, D. Jin, and E. M. Goldys, *Nanoscale*, 2013, **5**, 944.
 42. Y. Zhang, L. Zhang, R. Deng, J. Tian, Y. Zong, D. Jin, and X. Liu, *J. Am. Chem. Soc.*, 2014, **136**, 4893–4896.
 43. F. Wang and X. Liu, *Chem. Soc. Rev.*, 2009, **38**, 976.
 44. Z. Gu, L. Yan, G. Tian, S. Li, Z. Chai, and Y. Zhao, *Adv. Mater.*, 2013, **25**, 3758–3779.
 45. W. Feng, C. Han, and F. Li, *Adv. Mater.*, 2013, **25**, 5287–5303.
 46. H. Dong, L.-D. Sun, and C.-H. Yan, *Chem. Soc. Rev.*, 2014.
 47. D. M. Wu, A. García-Etxarri, A. Salleo, and J. A. Dionne, *J. Phys. Chem. Lett.*, 2014, **5**, 4020–4031.
 48. G. Liu, *Chem. Soc. Rev.*, 2014, 1–18.
 49. W. Zheng, P. Huang, D. Tu, E. Ma, and H. Zhu, *Chem. Soc. Rev.*, 2015.
 50. X. Li, F. Zhang, and D. Zhao, *Chem. Soc. Rev.*, 2015.
 51. D. J. Gargas, E. M. Chan, A. D. Ostrowski, S. Aloni, M. V. P. Altoe, E. S. Barnard, B. Sani, J. J. Urban, D. J. Milliron, B. E. Cohen, and P. J. Schuck, *Nat. Nanotech.*, 2014, **9**, 300–305.
 52. P. Andrew, *Science*, 2004, **306**, 1002–1005.
 53. H. Shpaisman, O. Niitsoo, I. Lubomirsky, and D. Cahen, *Sol. Energy Mater. Sol. Cells*, 2008, **92**, 1541–1546.
 54. M. Lunz, V. A. Gerard, Y. K. Gun'ko, V. Lesnyak, N. Gaponik, A. S. Sussha, A. L. Rogach, and A. L. Bradley, *Nano Lett.*, 2011, **11**, 3341–3345.
 55. S. Nie and S. R. Emory, *Science*, 1997, **275**, 1102–1106.

56. R. Esteban, M. Laroche, and J. J. Greffet, *J. Appl. Phys.*, 2009, **105**, 033107.
57. A. M. Michaels, M. Nirmal, and L. E. Brus, *J. Am. Chem. Soc.*, 1999, **121**, 9932–9939.
58. M. Saboktakin, X. Ye, U. K. Chettiar, N. Engheta, C. B. Murray, and C. R. Kagan, *ACS Nano*, 2013, **7**, 7186–7192.
59. J. R. Lakowicz, *Anal. Biochem.*, 2005, **337**, 171–194.
60. P. Yuan, Y. H. Lee, M. K. Gnanasammandhan, Z. Guan, Y. Zhang, and Q.-H. Xu, *Nanoscale*, 2012, **4**, 5132.
61. W. Zhang, F. Ding, and S. Y. Chou, *Adv. Mater.*, 2012, **24**, OP236–OP241.
62. Z. Q. Li, S. Chen, J. J. Li, Q. Q. Liu, Z. Sun, Z. B. Wang, and S. M. Huang, *J. Appl. Phys.*, 2012, **111**, 014310.
63. H. P. Paudel, L. Zhong, K. Bayat, M. F. Baroughi, S. Smith, C. Lin, C. Jiang, M. T. Berry, and P. S. May, *J. Phys. Chem. C*, 2011, **115**, 19028–19036.
64. W. Deng, L. Sudheendra, J. Zhao, J. Fu, D. Jin, I. M. Kennedy, and E. M. Goldys, *Nanotechnology*, 2011, **22**, 325604.
65. N. Liu, W. Qin, G. Qin, T. Jiang, and D. Zhao, *Chem. Commun.*, 2011, **47**, 7671.
66. H. Zhang, Y. Li, I. A. Ivanov, Y. Qu, Y. Huang, and X. Duan, *Angew. Chem. Int. Ed.*, 2010, **49**, 2865–2868.
67. S. Schietinger, T. Aichele, H.-Q. Wang, T. Nann, and O. Benson, *Nano Lett.*, 2010, **10**, 134–138.
68. H. Zhang, D. Xu, Y. Huang, and X. Duan, *Chem. Commun.*, 2010, **47**, 979.
69. Z. Li, L. Wang, Z. Wang, X. Liu, and Y. Xiong, *J. Phys. Chem. C*, 2011, **115**, 3291–3296.
70. E. Verhagen, A. Polman, and L. K. Kuipers, *Opt. Express*, 2008.
71. L. Novotny and B. Hecht, *Principles of Nano-Optics*, Cambridge University Press, 2012.
72. L. D. Barron and C. G. Gray, *J. Phys. A*, 1973, **6**, 59.
73. B. R. Judd, *Phys. Rev.*, 1962, **127**, 750.
74. G. S. Ofelt, *J. Chem. Phys.*, 1962, **37**, 511.
75. S. Hufner, *Optical Spectra of Transparent Rare Earth Compounds*, Academic Press, New York, 1978.
76. T. Förster, *Discuss. Faraday Soc.*, 1959, **27**, 7.
77. M. Inokuti and F. Hirayama, *J. Chem. Phys.*, 1965, **43**, 1978–1989.
78. J. Suyver, A. Aebischer, S. García-Revilla, P. Gerner, and H. Güdel, *Phys. Rev. B*, 2005, **71**, 125123.
79. B. Dong, B. Cao, Z. Feng, X. Wang, C. Li, and R. Hua, *Science in China Series G: Physics, Mechanics and Astronomy*, 2009, **52**, 1043–1046.
80. C. Strohhofer and A. Polman, *J. Appl. Phys.*, 2001, **90**, 4314.
81. J. Sommerdijk, *J. Lumin.*, 1971, **4**, 441–449.
82. E. Cantelar, J. A. Muñoz, J. A. Sanz-García, and F. Cusso, *J. Phys.: Condens. Matter*, 1998, **10**, 8893–8903.
83. J. D. Kingsley, G. E. Fenner, and S. V. Galginaitis, *Appl. Phys. Lett.*, 1969, **15**, 115–117.
84. B. Simondi-Teisseire, *Opt. Mater.*, 1996, **6**, 267–274.
85. D. C. Yeh, W. A. Sibley, M. Suscavage, and M. G. Drexhage, *J. Appl. Phys.*, 1987, **62**, 266–275.
86. B. Simondi-Teisseire, B. Viana, D. Vivien, and A. M. Lejus, *Opt. Mater.*, 1996, **6**, 267–274.
87. D. C. Yeh, W. A. Sibley, M. Suscavage, and M. G. Drexhage, *J. Appl. Phys.*, 1987, **62**,

- 266.
88. S. Taccheo, G. Sorbello, S. Longhi, and P. Laporta, *Opt. Quant. Electron.*, 1999, **31**, 249–262.
89. J. Nilsson, P. Scheer, and B. Jaskorzynska, *IEEE Photon. Technol. Lett.*, 1994, **6**, 383–385.
90. Q.-C. Sun, H. Mundoor, J. C. Ribot, V. Singh, I. I. Smalyukh, and P. Nagpal, *Nano Lett.*, 2014, **14**, 101–106.
91. C. Wyss, W. Lüthy, H. P. Weber, P. Rogin, and J. Hulliger, *Opt. Commun.*, 1997, **144**, 31–35.
92. D. Chen, Y. Wang, E. Ma, Y. Yu, and F. Liu, *Opt. Mater.*, 2007, **29**, 1693–1699.
93. D. Lu, S. K. Cho, S. Ahn, L. Brun, C. J. Summers, and W. Park, *ACS Nano*, 2014, **8**, 7780–7792.
94. L. D. Landau, J. S. Bell, M. J. Kearsley, L. P. Pitaevskii, E. M. Lifshitz, and J. B. Sykes, *Electrodynamics of Continuous Media*, Elsevier, 1984.
95. E. M. Purcell, *Phys. Rev.*, 1946, **69**, 681.
96. S. Haroche and D. Kleppner, *Phys. Today*, 1989, **42**, 24.
97. H. Iwase, D. Englund, and J. Vučković, *Opt. Express*, 2010, **18**, 16546–16560.
98. A. F. Koenderink, *Opt. Lett.*, 2010, **35**, 4208.
99. Y. Xu, J. S. Vučković, R. K. Lee, O. J. Painter, A. Scherer, and A. Yariv, *J. Opt. Soc. Am. B*, 1999, **16**, 465–474.
100. R. R. Chance, A. Prock, and R. Silbey, eds. I. Prigogine and S. A. Rice, *Adv. Chem. Phys.*, 1978, vol. 37, p. 1.
101. P. Anger, P. Bharadwaj, and L. Novotny, *Phys. Rev. Lett.*, 2006, **96**, 113002.
102. P. Andrew and W. L. Barnes, *Science*, 2000, **290**, 785–788.
103. H. T. Dung, L. Knöll, and D.-G. Welsch, *Phys. Rev. A*, 2002, **65**, 043813.
104. M. de Dood, J. Knoester, A. Tip, and A. Polman, *Phys. Rev. B*, 2005, **71**, 115102.
105. C. Blum, N. Zijlstra, A. Lagendijk, M. Wubs, A. P. Mosk, V. Subramaniam, and W. L. Vos, *Phys. Rev. Lett.*, 2012, **109**, 203601.
106. J. A. Gonzaga-Galeana and J. R. Zurita-Sánchez, *J. Chem. Phys.*, 2013, **139**, 244302.
107. J. I. Gersten and A. Nitzan, *Chem. Phys. Lett.*, 1984, **104**, 31–37.
108. X. M. Hua, J. I. Gersten, and A. Nitzan, *J. Chem. Phys.*, 1985, **83**, 3650.
109. A. Govorov, J. Lee, and N. Kotov, *Phys. Rev. B*, 2007, **76**, 125308.
110. M. Lunz, X. Zhang, V. A. Gerard, Y. K. Gun'ko, V. Lesnyak, N. Gaponik, A. S. Sussha, A. L. Rogach, and A. L. Bradley, *J. Phys. Chem. C*, 2012, **116**, 26529–26534.
111. Z.-K. Zhou, M. Li, Z.-J. Yang, X.-N. Peng, X.-R. Su, Z.-S. Zhang, J.-B. Li, N.-C. Kim, X.-F. Yu, L. Zhou, Z.-H. Hao, and Q.-Q. Wang, *ACS Nano*, 2010, **4**, 5003–5010.
112. T. Nakamura, M. Fujii, S. Miura, M. Inui, and S. Hayashi, *Phys. Rev. B*, 2006, **74**, 045302.
113. M. L. Viger, D. Brouard, and D. Boudreau, *J. Phys. Chem. C*, 2011, **115**, 2974–2981.
114. R. G. West and S. M. Sadeghi, *J. Phys. Chem. C*, 2012, **116**, 20496–20503.
115. X. Zhang, C. A. Marocico, M. Lunz, V. A. Gerard, Y. K. Gun'ko, V. Lesnyak, N. Gaponik, A. S. Sussha, A. L. Rogach, and A. L. Bradley, *ACS Nano*, 2014, **8**, 1273–1283.
116. Q. Luu, A. Hor, J. Fisher, R. B. Anderson, S. Liu, T.-S. Luk, H. P. Paudel, M. Farrokh Baroughi, P. S. May, and S. Smith, *J. Phys. Chem. C*, 2014, **118**, 3251–3257.
117. E. Verhagen, L. Kuipers, and A. Polman, *Opt. Express*, 2009, **17**, 14586–14598.
118. C. Genet and T. W. Ebbesen, *Nature*, 2007, **445**, 39–46.

119. N. J. Greybush, M. Saboktakin, X. Ye, C. Della Giovampaola, S. J. Oh, N. E. Berry, N. Engheta, C. B. Murray, and C. R. Kagan, *ACS Nano*, 2014, **8**, 9482–9491.
120. T. Som and B. Karmakar, *J. Opt. Soc. Am. B*, 2009, **26**, B21–B27.
121. T. Som and B. Karmakar, *Spectrochimica Acta A*, 2010, **75**, 640–646.
122. H. K. Dan, D. Zhou, R. Wang, Q. Jiao, Z. Yang, and Z. Song, *Ceramics International*, 2015, **41**, 2648–2653.
123. M. R. Dousti, R. J. Amjad, and Z. Mahraz, *J. Molecular Structure*, 2015, **1079**, 347–352.
124. D. M. da Silva, L. Kassab, and S. R. Lüthi, *App. Phys. Lett.*, 2007, **90**, 081913.
125. T. Som and B. Karmakar, *J. Appl. Phys.*, 2009.
126. S. Tirtha and K. Basudeb, *Solid State Sciences*, 2009, **11**, 1044–1051.
127. J. Ueda, S. Tanabe, and A. Ishida, *J. Non-Cryst. Sol.*, 2009, **355**, 1912–1915.
128. S. K. Singh, N. K. Giri, D. K. Rai, and S. B. Rai, *Solid State Sciences*, 2010, **12**, 1480–1483.
129. V. A. G. Rivera, S. P. A. Osorio, Y. Ledemi, D. Manzani, Y. Messaddeq, L. A. O. Nunes, and E. Marega, *Opt. Express*, 2010, **18**, 25321–25328.
130. Z. Pan, A. Ueda, R. Aga Jr., A. Burger, R. Mu, and S. H. Morgan, *J. Non-Cryst. Sol.*, 2010, **356**, 1097–1101.
131. J. Yang, B. Zhai, X. Zhao, Z. Wang, and H. Lin, *J. Phys. Chem. Sol.*, 2013, **74**, 772–778.
132. M. Reza Dousti, M. R. Sahar, R. J. Amjad, S. K. Ghoshal, A. Khorramnazari, A. Dordizadeh Basirabad, and A. Samavati, *Euro. Phys. J. D*, 2012, **66**, 237–6.
133. R. J. Amjad, M. R. Sahar, S. K. Ghoshal, and M. R. Dousti, *J. Lumin.*, 2012, **132**, 2714–2718.
134. Y. Sato, M. Terauchi, and K. Adachi, *J. Appl. Phys.*, 2012, **112**, 074308.
135. M. R. Dousti, M. R. Sahar, S. K. Ghoshal, R. J. Amjad, and R. Arifin, *J. Non-Cryst. Sol.*, 2012, **358**, 2939–2942.
136. C. F. Bohren and D. R. Huffman, *Absorption and Scattering of Light by Small Particles*, JWILEY-VCH Verlag GmbH & Co. KGaA, Weinheim, 2008.
137. P. B. Johnson and R. W. Christy, *Phys. Rev. B*, 1972, **6**, 4370.
138. M. R. Dousti, *J. Appl. Phys.*, 2013, **114**, 113105.
139. M. Saboktakin, X. Ye, S. J. Oh, S.-H. Hong, A. T. Fafarman, U. K. Chettiar, N. Engheta, C. B. Murray, and C. R. Kagan, *ACS Nano*, 2012, **6**, 8758–8766.
140. S. Liu, G. Chen, T. Y. Ohulchanskyy, M. T. Swihart, and P. N. Prasad, *Theranostics*, 2013, **3**, 275–281.
141. P. Kannan, F. Abdul Rahim, R. Chen, X. Teng, L. Huang, H. Sun, and D.-H. Kim, *ACS Appl. Mater. Interfaces*, 2013, **5**, 3508–3513.
142. N. Tu and L. Wang, *Chem. Commun.*, 2013, **49**, 6319–6321.
143. L. P. Qian, L. H. Zhou, H.-P. Too, and G.-M. Chow, *J. Nanopart. Res.*, 2011, **13**, 499–510.
144. Z. Q. Li, X. D. Li, Q. Q. Liu, X. H. Chen, Z. Sun, C. Liu, X. J. Ye, and S. M. Huang, *Nanotechnology*, 2012, **23**, 025402.
145. P. Zhao, Y. Zhu, X. Yang, K. Fan, J. Shen, and C. Li, *RSC Advances*, 2012, **2**, 10592–10597.
146. H. Xing, W. Bu, S. Zhang, X. Zheng, M. Li, F. Chen, Q. He, L. Zhou, W. Peng, Y. Hua, and J. Shi, *Biomaterials*, 2012, **33**, 1079–1089.
147. H. Zhang, D. Xu, Y. Huang, and X. Duan, *Chem. Commun.*, 2011, **47**, 979–981.

148. P. Zhao, Y. Zhu, X. Yang, X. Jiang, J. Shen, and C. Li, *J. Mater. Chem. A*, 2014, **2**, 16523–16530.
149. W. Ge, X. R. Zhang, M. Liu, Z. W. Lei, R. J. Knize, and Y. Lu, *Theranostics*, 2013, **3**, 282–288.
150. T. Jiang, J. Li, W. Qin, and J. Zhou, *J. Lumin.*, 2014, **156**, 164–169.
151. Y. Song, G. Liu, X. Dong, J. Wang, W. Yu, and J. Li, *RSC Advances*, 2014, **4**, 62802–62808.
152. T. Jiang, Y. Liu, S. Liu, N. Liu, and W. Qin, *J. Col. Interf. Sci.*, 2012, **377**, 81–87.
153. P. Anger, P. Bharadwaj, and L. Novotny, *Phys. Rev. Lett.*, 2006, **96**, 113002.
154. W. Xu, S. Xu, Y. Zhu, T. Liu, X. Bai, B. Dong, L. Xu, and H. Song, *Nanoscale*, 2012, **4**, 6971–6973.
155. W. Feng, L.-D. Sun, and C.-H. Yan, *Chem. Commun.*, 2009, 4393.
156. Zhang-Fan, G. B. Braun, Y. Shi, Y. Zhang, X. Sun, N. O. Reich, D. Zhao, and G. Stucky, *J. Am. Chem. Soc.*, 2010, **132**, 2850–2851.
157. J. Shen, Z. Q. Li, Y. R. Chen, X. H. Chen, Y. W. Chen, Z. Sun, and S. M. Huang, *Appl. Surf. Sci.*, 2013, **270**, 712–717.
158. Y. Ding, X. Zhang, H. Gao, S. Xu, C. Wei, and Y. Zhao, *J. Lumin.*, 2014, **147**, 72–76.
159. E. He, H. Zheng, J. Dong, W. Gao, Q. Han, J. Li, L. Hui, Y. Lu, and H. Tian, *Nanotechnology*, 2014, **25**, 045603.
160. J. Liao, Z. Yang, S. Lai, B. Shao, J. Li, J. Qiu, Z. Song, and Y. Yang, *J. Phys. Chem. C*, 2014, **118**, 17992–17999.
161. D. Yin, C. Wang, J. Ouyang, X. Zhang, Z. Jiao, Y. Feng, K. Song, B. Liu, X. Cao, L. Zhang, Y. Han, and M. Wu, *ACS Appl. Mater. Interfaces*, 2014, **6**, 18480–18488.
162. P. Ramasamy and J. Kim, *Chem. Commun.*, 2014, **50**, 879–881.
163. W. Xu, Y. Zhu, X. Chen, J. Wang, L. Tao, S. Xu, T. Liu, and H. Song, *Nano Res.*, 2013, **6**, 795–807.
164. S. Chawla, M. Parvaz, V. Kumar, and Z. Buch, *New J. Chem.*, 2013, **37**, 3991–3997.
165. T. Aisaka, M. Fujii, and S. Hayashi, *Appl. Phys. Lett.*, 2008, **92**, 132105.
166. N. Halas, *Optics and Photonics News*, 2002, **13**, 26–30.
167. J. H. Lee, Q. Wu, and W. Park, *J. Mater. Res.*, 2006, **21**, 3215–3221.
168. J. H. Lee and W. Park, *Func. Mater. Lett.*, 2008, **1**, 65–69.
169. M. Fujii, T. Nakano, K. Imakita, and S. Hayashi, *J. Phys. Chem. C*, 2013, **117**, 1113–1120.
170. A. Priyam, N. M. Idris, and Y. Zhang, *J. Mater. Chem.*, 2012, **22**, 960–965.
171. P. Kannan, F. A. Rahim, X. Teng, R. Chen, H. Sun, L. Huang, and D.-H. Kim, *RSC Advances*, 2013, **3**, 7718.
172. W. Xu, X. Min, X. Chen, Y. Zhu, P. Zhou, S. Cui, S. Xu, L. Tao, and H. Song, *Sci. Rep.*, 2014, **4**, 5087.
173. X. Zhang, C. A. Marocico, M. Lunz, V. A. Gerard, Y. K. Gun'ko, V. Lesnyak, N. Gaponik, A. S. Sussha, A. L. Rogach, and A. L. Bradley, *ACS Nano*, 2012, **6**, 9283–9290.
174. L. D. DeLoach, S. A. Payne, L. L. Chase, L. K. Smith, W. L. Kway, and W. F. Krupke, *IEEE J. Quantum Electron.*, 1993, **29**, 1179–1191.
175. L. Sudheendra, V. Ortalan, S. Dey, N. D. Browning, and I. M. Kennedy, *Chem. Mater.*, 2011, **23**, 2987–2993.
176. G. Blasse and B. C. Grabmaier, *Luminescent Materials*, Springer Verlag, 1994.
177. J. M. F. van Dijk, *J. Chem. Phys.*, 1983, **78**, 5317.

178. L. Cheng, K. Yang, Y. Li, X. Zeng, M. Shao, S.-T. Lee, and Z. Liu, *Biomaterials*, 2012, **33**, 2215–2222.
179. F. Wang, D. Banerjee, Y. Liu, X. Chen, and X. Liu, *Analyst*, 2010, **135**, 1839.
180. B. Dong, S. Xu, J. Sun, S. Bi, D. Li, X. Bai, Y. Wang, L. Wang, and H. Song, *J. Mater. Chem.*, 2011, **21**, 6193.
181. J. Shan, W. Kong, R. Wei, N. Yao, and Y. Ju, *J. Appl. Phys.*, 2010, **107**, 054901.
182. X. Bai, H. Song, G. Pan, Y. Lei, T. Wang, X. Ren, S. Lu, B. Dong, Q. Dai, and L. Fan, *J. Phys. Chem. C*, 2007, **111**, 13611–13617.
183. M. Kauranen and A. V. Zayats, *Nat. Photon.*, 2012, **6**, 737–748.
184. W. Shockley and H. J. Queisser, *J. Appl. Phys.*, 1961, **32**, 510–519.
185. T. Trupke, A. Shalav, B. S. Richards, P. Würfel, and M. A. Green, *Sol. Energy Mater. Sol. Cells*, 2006, **90**, 3327–3338.
186. A. Shalav, B. S. Richards, and M. A. Green, *Sol. Energy Mater. Sol. Cells*, 2007, **91**, 829–842.
187. W. G. van Sark, J. de Wild, J. K. Rath, A. Meijerink, and R. E. Schropp, *Nanoscale Res. Lett.*, 2013, **8**, 81.
188. T. W. Schmidt and F. N. Castellano, *J. Phys. Chem. Lett.*, 2014, **5**, 4062–4072.
189. J. Wang, T. Ming, Z. Jin, J. Wang, L.-D. Sun, and C.-H. Yan, *Nat. Commun.*, 2014, **5**, 5669.
190. F. van de Rijke, H. Zijlmans, S. Li, T. Vail, A. K. Raap, R. S. Niedbala, and H. J. Tanke, *Nat. Biotechnol.*, 2001, **19**, 273–276.